

## GALAXY CLUSTERS DISCOVERED VIA THE SUNYAEV–ZEL'DOVICH EFFECT IN THE FIRST 720 SQUARE DEGREES OF THE SOUTH POLE TELESCOPE SURVEY

C. L. REICHARDT<sup>1</sup>, B. STALDER<sup>2</sup>, L. E. BLEEM<sup>3,4</sup>, T. E. MONTROY<sup>5</sup>, K. A. AIRD<sup>6</sup>, K. ANDERSSON<sup>7,8</sup>, R. ARMSTRONG<sup>9</sup>, M. L. N. ASHBY<sup>2</sup>, M. BAUTZ<sup>8</sup>, M. BAYLISS<sup>10</sup>, G. BAZIN<sup>7,11</sup>, B. A. BENSON<sup>3,12</sup>, M. BRODWIN<sup>13</sup>, J. E. CARLSTROM<sup>3,4,12,14,15</sup>, C. L. CHANG<sup>3,12,15</sup>, H. M. CHO<sup>16</sup>, A. CLOCCHIATTI<sup>17</sup>, T. M. CRAWFORD<sup>3,14</sup>, A. T. CRITES<sup>3,14</sup>, T. DE HAAN<sup>18</sup>, S. DESAI<sup>7,11</sup>, M. A. DOBBS<sup>18</sup>, J. P. DUDLEY<sup>18</sup>, R. J. FOLEY<sup>2</sup>, W. R. FORMAN<sup>2</sup>, E. M. GEORGE<sup>1</sup>, M. D. GLADDERS<sup>3,14</sup>, A. H. GONZALEZ<sup>19</sup>, N. W. HALVERSON<sup>20</sup>, N. L. HARRINGTON<sup>1</sup>, F. W. HIGH<sup>3,14</sup>, G. P. HOLDER<sup>18</sup>, W. L. HOLZAPFEL<sup>1</sup>, S. HOOVER<sup>3,12</sup>, J. D. HRUBES<sup>6</sup>, C. JONES<sup>2</sup>, M. JOY<sup>21</sup>, R. KEISLER<sup>3,4</sup>, L. KNOX<sup>22</sup>, A. T. LEE<sup>1,23</sup>, E. M. LEITCH<sup>3,14</sup>, J. LIU<sup>7,11</sup>, M. LUEKER<sup>1,24</sup>, D. LUONG-VAN<sup>6</sup>, A. MANTZ<sup>3</sup>, D. P. MARRONE<sup>25</sup>, M. McDONALD<sup>8</sup>, J. J. McMAHON<sup>3,12,26</sup>, J. MEHL<sup>3,14</sup>, S. S. MEYER<sup>3,4,12,14</sup>, L. MOCANU<sup>3,14</sup>, J. J. MOHR<sup>7,11,27</sup>, S. S. MURRAY<sup>2</sup>, T. NATOLI<sup>3,4</sup>, S. PADIN<sup>3,14,24</sup>, T. PLAGGE<sup>3,14</sup>, C. PRYKE<sup>28</sup>, A. REST<sup>29</sup>, J. RUEL<sup>10</sup>, J. E. RUHL<sup>5</sup>, B. R. SALIWANCHIK<sup>5</sup>, A. SARO<sup>7</sup>, J. T. SAYRE<sup>5</sup>, K. K. SCHAFFER<sup>3,12,30</sup>, L. SHAW<sup>18,31</sup>, E. SHIROKOFF<sup>1,24</sup>, J. SONG<sup>26</sup>, H. G. SPIELER<sup>23</sup>, Z. STANISZEWSKI<sup>5</sup>, A. A. STARK<sup>2</sup>, K. STORY<sup>3,4</sup>, C. W. STUBBS<sup>2,10</sup>, R. ŠUHADA<sup>7</sup>, A. VAN ENGELEN<sup>18</sup>, K. VANDERLINDE<sup>18</sup>, J. D. VIEIRA<sup>3,4,24</sup>, A. VIKHLININ<sup>2</sup>, R. WILLIAMSON<sup>3,14</sup>, O. ZAHN<sup>1,32</sup>, AND A. ZENTENO<sup>7,11</sup>

<sup>1</sup> Department of Physics, University of California, Berkeley, CA 94720, USA; [cr@bolo.berkeley.edu](mailto:cr@bolo.berkeley.edu)

<sup>2</sup> Harvard-Smithsonian Center for Astrophysics, 60 Garden Street, Cambridge, MA 02138, USA

<sup>3</sup> Kavli Institute for Cosmological Physics, University of Chicago, 5640 South Ellis Avenue, Chicago, IL 60637, USA

<sup>4</sup> Department of Physics, University of Chicago, 5640 South Ellis Avenue, Chicago, IL 60637, USA

<sup>5</sup> Physics Department, Center for Education and Research in Cosmology and Astrophysics, Case Western Reserve University, Cleveland, OH 44106, USA

<sup>6</sup> University of Chicago, 5640 South Ellis Avenue, Chicago, IL 60637, USA

<sup>7</sup> Department of Physics, Ludwig-Maximilians-Universität, Scheinerstr. 1, D-81679 München, Germany

<sup>8</sup> MIT Kavli Institute for Astrophysics and Space Research, Massachusetts Institute of Technology, 77 Massachusetts Avenue, Cambridge, MA 02139, USA

<sup>9</sup> National Center for Supercomputing Applications, University of Illinois, 1205 West Clark Street, Urbana, IL 61801, USA

<sup>10</sup> Department of Physics, Harvard University, 17 Oxford Street, Cambridge, MA 02138, USA

<sup>11</sup> Excellence Cluster Universe, Boltzmannstr. 2, D-85748 Garching, Germany

<sup>12</sup> Enrico Fermi Institute, University of Chicago, 5640 South Ellis Avenue, Chicago, IL 60637, USA

<sup>13</sup> Department of Physics and Astronomy, University of Missouri, 5110 Rockhill Road, Kansas City, MO 64110, USA

<sup>14</sup> Department of Astronomy and Astrophysics, University of Chicago, 5640 South Ellis Avenue, Chicago, IL 60637, USA

<sup>15</sup> Argonne National Laboratory, 9700 South Cass Avenue, Argonne, IL 60439, USA

<sup>16</sup> NIST Quantum Devices Group, 325 Broadway Mailcode 817.03, Boulder, CO 80305, USA

<sup>17</sup> Departamento de Astronomía y Astrofísica, PUC Casilla 306, Santiago 22, Chile

<sup>18</sup> Department of Physics, McGill University, 3600 Rue University, Montreal, Quebec H3A 2T8, Canada

<sup>19</sup> Department of Astronomy, University of Florida, Gainesville, FL 32611, USA

<sup>20</sup> Department of Astrophysical and Planetary Sciences and Department of Physics, University of Colorado, Boulder, CO 80309, USA

<sup>21</sup> Department of Space Science, VP62, NASA Marshall Space Flight Center, Huntsville, AL 35812, USA

<sup>22</sup> Department of Physics, University of California, One Shields Avenue, Davis, CA 95616, USA

<sup>23</sup> Physics Division, Lawrence Berkeley National Laboratory, Berkeley, CA 94720, CA

<sup>24</sup> Astronomy Department, California Institute of Technology, 1200 East California Boulevard, Pasadena, CA 91125, USA

<sup>25</sup> Steward Observatory, University of Arizona, 933 North Cherry Avenue, Tucson, AZ 85721

<sup>26</sup> Department of Physics, University of Michigan, 450 Church Street, Ann Arbor, MI 48109, USA

<sup>27</sup> Max-Planck-Institut für extraterrestrische Physik, Giessenbachstr., D-85748 Garching, Germany

<sup>28</sup> Physics Department, University of Minnesota, 116 Church Street S.E., Minneapolis, MN 55455, USA

<sup>29</sup> Space Telescope Science Institute, 3700 San Martin Drive, Baltimore, MD 21218, USA

<sup>30</sup> Liberal Arts Department, School of the Art Institute of Chicago, 112 S Michigan Avenue, Chicago, IL 60603, USA

<sup>31</sup> Department of Physics, Yale University, P.O. Box 208210, New Haven, CT 06520-8120, USA

<sup>32</sup> Berkeley Center for Cosmological Physics, Department of Physics, University of California, and Lawrence Berkeley National Labs, Berkeley, CA 94720, USA

Received 2012 March 26; accepted 2012 December 10; published 2013 January 16

### ABSTRACT

We present a catalog of galaxy cluster candidates, selected through their Sunyaev–Zel'dovich (SZ) effect signature in the first 720 deg<sup>2</sup> of the South Pole Telescope (SPT) survey. This area was mapped with the SPT in the 2008 and 2009 austral winters to a depth of  $\sim 18 \mu\text{K}_{\text{CMB}}$ -arcmin at 150 GHz; 550 deg<sup>2</sup> of it was also mapped to  $\sim 44 \mu\text{K}_{\text{CMB}}$ -arcmin at 95 GHz. Based on optical imaging of all 224 candidates and near-infrared imaging of the majority of candidates, we have found optical and/or infrared counterparts for 158, which we then classify as confirmed galaxy clusters. Of these 158 clusters, 135 were first identified as clusters in SPT data, including 117 new discoveries reported in this work. This catalog triples the number of confirmed galaxy clusters discovered through the SZ effect. We report photometrically derived (and in some cases spectroscopic) redshifts for confirmed clusters and redshift lower limits for the remaining candidates. The catalog extends to high redshift with a median redshift of  $z = 0.55$  and maximum confirmed redshift of  $z = 1.37$ . Forty-five of the clusters have counterparts in the *ROSAT* bright or faint source catalogs from which we estimate X-ray fluxes. Based on simulations, we expect the catalog to be nearly 100% complete above  $M_{500} \approx 5 \times 10^{14} M_{\odot} h_{70}^{-1}$  at  $z \gtrsim 0.6$ . There are 121 candidates detected at signal-to-noise ratio greater than five, at which the catalog purity is measured to be 95%. From this high-purity subsample, we exclude the  $z < 0.3$  clusters and use the remaining 100 candidates to improve cosmological constraints following the method presented by Benson et al. Adding the cluster data to CMB + BAO +  $H_0$  data leads to a preference for non-zero neutrino masses while only slightly reducing the upper limit on the sum of

neutrino masses to  $\sum m_\nu < 0.38$  eV (95% CL). For a spatially flat  $\Lambda$ CDM cosmological model, the addition of this catalog to the CMB + BAO +  $H_0$  + SNe results yields  $\sigma_8 = 0.807 \pm 0.027$  and  $w = -1.010 \pm 0.058$ , improving the constraints on these parameters by a factor of 1.4 and 1.3, respectively. The larger cluster catalog presented in this work leads to slight improvements in cosmological constraints from those presented by Benson et al. These cosmological constraints are currently limited by uncertainty in the cluster mass calibration, not the size or quality of the cluster catalog. A multi-wavelength observation program to improve the cluster mass calibration will make it possible to realize the full potential of the final 2500 deg<sup>2</sup> SPT cluster catalog to constrain cosmology.

*Key words:* cosmic background radiation – cosmology: observations – galaxies: clusters: individual – large-scale structure of universe

*Online-only material:* color figures, machine-readable table

## 1. INTRODUCTION

Galaxy clusters are the largest collapsed objects in the universe, and their abundance is exponentially sensitive to the growth of structure. Measurements of the abundance of galaxy clusters as a function of mass and redshift have the potential to significantly improve current constraints on cosmological parameters, including the equation of state of dark energy and the sum of the neutrino masses (Wang & Steinhardt 1998; Haiman et al. 2001; Holder et al. 2001; Battye & Weller 2003; Molnar et al. 2004; Wang et al. 2004, 2005; Lima & Hu 2007; Shimon et al. 2011). To achieve this objective, a sample of galaxy clusters must have a well understood selection function, good mass estimates, and wide redshift extent.

Most known galaxy clusters have been identified by their optical properties or from their X-ray emission. Clusters of galaxies contain anywhere from tens to thousands of galaxies, but these galaxies account for a small fraction of the total baryonic mass in a cluster (see, e.g., Allen et al. 2011 for a review). Most of the baryons in clusters are contained in the intra-cluster medium (ICM), the hot ( $10^7$ – $10^8$  K) X-ray-emitting plasma that pervades cluster environments.

Sunyaev & Zel’dovich (1972) noted that such a plasma would also interact with cosmic microwave background (CMB) photons via inverse Compton scattering, causing a small spectral distortion of the CMB along the line of sight to a cluster. This is called the thermal Sunyaev–Zel’dovich (SZ) effect.<sup>33</sup> The amplitude of the spectral distortion at a given position on the sky is proportional to the integrated electron pressure along the line of sight. Therefore, the integrated thermal SZ (tSZ) flux is a direct measure of the total thermal energy of the ICM, and the SZ flux is thus expected to be a robust proxy for total cluster mass (Barbosa et al. 1996; Holder & Carlstrom 2001; Motl et al. 2005). Additionally, the SZ surface brightness is independent of redshift. As a result, SZ surveys with sufficient angular resolution have the potential to deliver nearly mass-limited cluster samples over a wide redshift range (Carlstrom et al. 2002). Such a cluster sample can provide a growth-based test of dark energy to complement the distance-based tests provided by supernovae (e.g., Riess et al. 1998; Perlmutter et al. 1999); it can also probe the sum of the neutrino masses. Recent results (e.g., Vikhlinin et al. 2009b; Mantz et al. 2010; Benson et al. 2011) have demonstrated the power of such tests to constrain cosmological models and parameters.

However, the SZ signal is faint, exceeding a few hundred  $\mu$ K for only the most massive (and rare) galaxy clusters. As a result, experiments have only recently achieved the requisite

sensitivity to discover previously unknown galaxy clusters. Since the first discovery of clusters using South Pole Telescope (SPT) data (Staniszewski et al. 2009), SZ-selected galaxy cluster catalogs have been produced by the SPT, Atacama Cosmology Telescope (ACT), and Planck collaborations (Vanderlinde et al. 2010; Williamson et al. 2011; Marriage et al. 2011; Planck Collaboration et al. 2011). In total, roughly 40 previously unknown clusters discovered via the SZ effect have been published to date.

This is the third SPT cluster catalog and fourth SPT cosmological analysis based on galaxy cluster counts. Vanderlinde et al. (2010, hereafter V10) presented the first SZ-selected catalog, consisting of 21 optically confirmed galaxy clusters found in 2008 SPT data. V10 also investigated the cosmological implications of these clusters, using a simulation-calibrated mass scaling relation. The second SPT cluster catalog and cosmological analysis (Williamson et al. 2011, hereafter W11) used the most massive galaxy clusters discovered in the entire 2500 deg<sup>2</sup> SPT survey region to test for non-Gaussianity and consistency with  $\Lambda$ CDM. In the third analysis, Benson et al. (2011, hereafter B11) developed a method to combine X-ray data with the SZ observations, and thereby improve the cluster mass estimates. B11 used this method to improve the cosmological constraints from the V10 cluster sample.

In this work, we present a catalog of 224 SZ-identified galaxy cluster candidates above  $4.5\sigma$  from the first 720 deg<sup>2</sup> of the SPT survey. Using follow-up optical imaging of all candidates and near-infrared (NIR) imaging for a subset, we estimate redshifts for 158 of the candidates and calculate lower redshift limits for the remaining candidates, which are either too distant to identify with current optical/NIR observations or are spurious detections in the SPT data. The details of the optical and NIR data and redshift estimates are given in a companion paper (Song et al. 2012b, hereafter S12). Here we summarize the observations and report the resulting redshifts. The clusters with clear optical/NIR counterparts include 117 new discoveries, which increases the number of clusters discovered with the SPT to 144 and triples the total number of SZ-discovered clusters. Simulations are used to characterize the SPT cluster selection function. We combine the cluster list with the improved mass scaling relation from B11 to improve cosmological constraints on large-scale structure, neutrino masses, and the dark energy equation of state.

The paper is organized as follows. We describe the observations and map making in Section 2. The extraction of galaxy clusters from the maps is detailed in Section 3. The optical follow-up campaign and the resulting redshifts are presented in Section 4. In Section 5, we present the complete catalog of galaxy cluster candidates. We review the B11 method for

<sup>33</sup> In this work, “SZ effect” will refer to the thermal SZ effect unless specifically noted as the kinetic SZ effect.

simultaneously constraining cosmological and scaling relation parameters in Section 6, and we discuss the cosmological constraints from this cluster catalog and prospects for future improvement in Section 7 before concluding in Section 8.

## 2. OBSERVATIONS AND DATA REDUCTION

### 2.1. Telescope and Observations

SPT is a 10 m telescope designed to survey a large area of the sky at millimeter wavelengths with arcminute angular resolution (Ruhl et al. 2004; Padin et al. 2008; Carlstrom et al. 2011). The first SPT receiver was a three-band (95, 150, and 220 GHz) bolometer camera optimized for studying the primary CMB anisotropy and the tSZ effect. From the time the SPT was commissioned through the end of 2011, the majority of observing time was spent on the recently completed 2500 deg<sup>2</sup> SPT survey. The cluster catalog presented in this paper is derived from the first 720 deg<sup>2</sup> of this survey. This area was observed during the Austral winters of 2008 and 2009. In addition to the early SPT galaxy cluster results discussed in Section 1, science results from early subsets of the survey data have included measurements of the primary and secondary CMB anisotropy (Keisler et al. 2011; Lueker et al. 2010; Shirokoff et al. 2011; Reichardt et al. 2012), a measurement of gravitational lensing of the CMB (van Engelen et al. 2012), and the discovery of a new population of extremely bright submillimeter galaxies (Vieira et al. 2010).

For cluster-finding, we use data from the SPT 95 GHz and 150 GHz frequency bands. The effective band centers for a non-relativistic tSZ spectrum are 97.6 GHz and 152.9 GHz. The 220 GHz band is centered near the tSZ null, so it contains effectively no SZ cluster signal; the 220 GHz data is also too shallow to effectively subtract the CMB. In the 2008 observing season, the 480 detectors at 150 GHz performed well, but the 95 GHz detectors did not meet specifications. The receiver was reconfigured for the 2009 observing season with 640 detectors at 150 GHz and 160 new detectors at 95 GHz. We observed roughly 170 deg<sup>2</sup> in two fields in 2008 and 550 deg<sup>2</sup> in three fields in 2009. Each field was observed to a minimum depth of 18  $\mu$ K<sub>CMB</sub>-arcmin at 150 GHz.<sup>34</sup> The 2009 fields were observed to a minimum depth of 44  $\mu$ K<sub>CMB</sub>-arcmin at 95 GHz. The SPT map of the first of the two 2008 fields is publicly available (Schaffer et al. 2011).

The standard operating mode of the SPT is to observe a target field by scanning back and forth in azimuth across the field followed by a step in elevation (Schaffer et al. 2011). One field (RA21HDEC-50) was observed with a hybrid scan strategy including scans at both constant elevation and constant azimuth. This scan strategy changes the filtered point spread function for this field compared to the rest of the data, which affects the SPT signal-to-noise ratio (S/N) to cluster mass scaling relations presented in Section 6.2.

The SPT beams have been measured using a combination of bright active galactic nuclei (AGNs) in the survey fields and targeted observations of planets (Shirokoff et al. 2011; Keisler et al. 2011). The SPT beam can be described by a main lobe and a diffuse sidelobe. For compact sources such as galaxy clusters, the effect of the sidelobe is degenerate with a calibration factor, and we choose to fold it into the calibration. The SPT main lobe beam is well-described by a Gaussian with FWHM = 1'6 and

1'19 at 95 and 150 GHz, respectively. The 2009 data in this work are calibrated using observations of RCW38, a galactic H II region (Staniszewski et al. 2009, W11), while the 2008 data are calibrated by cross-correlating dedicated SPT observations of large patches of sky with *WMAP* observations of those same regions (V10).

The pointing model is determined using daily observations of galactic H II regions and sensors on the telescope structure sensitive to temperature and mechanical movement (Schaffer et al. 2011). The final pointing in the maps is checked against the positions of radio sources in the Australia Telescope 20 GHz survey (AT20G, Murphy et al. 2010), which has positional accuracy to better than 1 arcsec. The absolute SPT pointing measured in this way is accurate to 3 arcsec. The rms pointing uncertainty in the maps is 7 arcsec.

### 2.2. Map Making

The map-making algorithm for the SPT data has been described in detail in Lueker et al. (2010), Shirokoff et al. (2011), and V10. In overview, the first step is to apply a relative calibration to the time-ordered data (TOD) and then bandpass filter the TOD. Correlated atmospheric signals are removed by subtracting the mean signal across a set of adjacent bolometers. We mask bright point sources detected at  $>5\sigma$  at 150 GHz ( $>\sim 6$  mJy) before filtering. The pointing for each detector is reconstructed, and the data from each detector are co-added into a map with inverse-noise weighting.

The maps (and cluster list) for the 2008 season are identical to those presented by V10. Maps for the 2009 season have several small differences in the filtering detailed below.

1. In V10, the bandpass filter was set by a high-pass filter (HPF) at 0.25 Hz and a low-pass filter at 25 Hz. In 2009, different fields were observed at different scan speeds, so we choose to define the HPF with respect to angular multipole  $\ell$ . The HPF of the 2009 data is at  $\ell = 400$ ; the V10 HPF corresponds to  $\ell \simeq 350$ . As in V10, the HPF is implemented by removing a set of sines and cosines from each scan across the field. We supplement the Fourier mode removal by first fitting and removing a 9th order Legendre polynomial from each scan. The higher order (V10 used first order) is necessitated by the large atmospheric modulation introduced by the subset of observations which scan in elevation. Depending on the observation, this filter acts as a high-pass filter in either the R.A. or decl. direction.
2. V10 removed both the mean and slope across the two-dimensional array of all detectors at a single frequency. The 2009 data have four times as many 150 GHz detectors as 95 GHz detectors so the V10 scheme would result in different common mode removal at each frequency. Instead, we follow the treatment in Shirokoff et al. (2011) and remove the mean across sets of neighboring detectors. The 150 GHz detectors are divided into four sets based on their position in the focal plane and the 95 GHz detectors are treated as a single set. This filter set choice produces nearly identical filtering at 95 and 150 GHz.

## 3. CLUSTER EXTRACTION

The procedure used in this work to identify SZ galaxy cluster candidates is identical to that used by W11. We summarize the procedure here and refer the reader to W11 for more details.

Most of the SPT fields have been observed in three frequency bands, centered at 95, 150, and 220 GHz. (Roughly one-quarter

<sup>34</sup> Throughout this work, the unit  $K_{\text{CMB}}$  refers to equivalent fluctuations in the CMB temperature, i.e., the temperature fluctuation of a 2.73 K blackbody that would be required to produce the same power fluctuation.

of the sky area considered in this work was observed in 2008 without 95 GHz coverage.) Each map at a given observing frequency contains contributions from multiple astrophysical signals, and each signal has its own spatial and spectral properties. Because the maps are calibrated in CMB fluctuation temperature units, primary CMB fluctuations and the (small) signal from the kinetic SZ (kSZ) effect contribute equally to all frequencies. Emissive radio galaxies appear in all frequencies with a falling spectral index, while dusty, star-forming galaxies appear with a rising spectral index. Most notably, the 95 GHz and 150 GHz maps contain the tSZ effect signal from galaxy clusters. Because the spectral signature of the tSZ effect is known (up to a small relativistic correction), and because we can roughly predict the spatial profile of the tSZ signal from galaxy clusters, we can combine the maps from the different bands, weighted in spatial frequency space by the expected cluster profile, to maximize the S/N of the tSZ effect from clusters.

Under certain assumptions about the noise, the astrophysical contaminants, and the source profile, it can be shown (e.g., Melin et al. 2006) that the optimal way to extract a cluster-shaped tSZ signal from our data is to construct a simultaneous spatial-spectral filter, given by

$$\psi(k_x, k_y, \nu_i) = \sigma_\psi^{-2} \sum_j \mathbf{N}_{ij}^{-1}(k_x, k_y) f_{\text{SZ}}(\nu_j) S_{\text{filt}}(k_x, k_y, \nu_j). \quad (1)$$

Here,  $\sigma_\psi^{-2}$  is the predicted variance in the filtered map

$$\sigma_\psi^{-2} = \sum_{i,j} f_{\text{SZ}}(\nu_i) S_{\text{filt}}(k_x, k_y, \nu_i) \mathbf{N}_{ij}^{-1}(k_x, k_y) \times f_{\text{SZ}}(\nu_j) S_{\text{filt}}(k_x, k_y, \nu_j), \quad (2)$$

$S_{\text{filt}}$  is the assumed cluster profile convolved with the instrument beam and any filtering performed in the map-making step,  $\mathbf{N}_{ij}$  is the band-band noise covariance matrix (including contributions from astrophysical signals other than cluster tSZ), and  $f_{\text{SZ}}$  encodes the frequency scaling of the tSZ effect relative to primary CMB fluctuations (e.g., Sunyaev & Zel'dovich 1980).

As in W11, our model for the astrophysical contribution to  $\mathbf{N}_{ij}$  is a combination of primary and lensed CMB fluctuations, point sources below the SPT detection threshold, kSZ, and tSZ from clusters below the SPT detection threshold. The assumptions about the spatial and spectral shapes of each component are identical to those in W11. As in all previous SPT cluster survey publications, the assumed cluster profile is described by a projected spherical isothermal  $\beta$ -model (Cavaliere & Fusco-Femiano 1976), with  $\beta$  fixed to 1. Varying the assumed cluster profile leads to only minor (percent-level) changes in the observed S/N. Twelve different matched filters were constructed and applied to the data, each with a different core radius, spaced evenly between 0.25 and 3.0. As in previous work, point sources detected above  $5\sigma$  at 150 GHz were masked out to a radius of  $4'$ , with the value inside that radius set to the average of the surrounding pixels from  $4' < r < 4.5'$ . Furthermore, cluster detections within  $8'$  of one of these  $>5\sigma$  point sources were rejected. Clusters were extracted from the filtered maps with the process used in all previous SPT cluster work and described by V10. As in V10 and W11, we refer to the detection significance maximized across all twelve matched filters as  $\xi$ , and we use  $\xi$  as the primary SZ observable. As in W11, we use only 95 (where available) and 150 GHz data to extract clusters, as adding the 220 GHz data does not result in measurable improvement in cluster yield (see W11 for details).

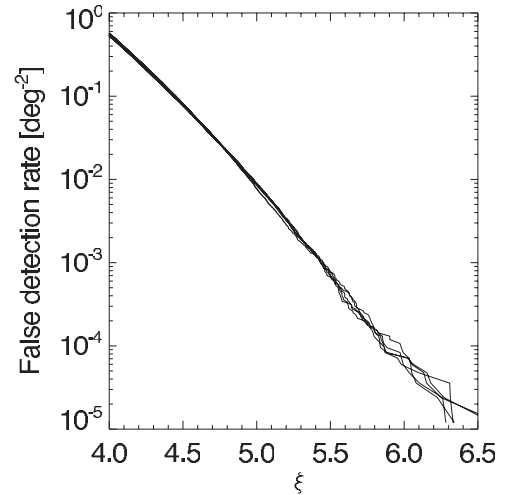


**Figure 1.** Simulated cumulative false detection rates, for each of the five fields, as a function of lower S/N threshold ( $\xi$ ). No significant differences between the fields are observed. The vertical axis shows the number density of false detections above a given S/N.

### 3.1. Simulations

We use simulations to determine priors on the SZ scaling relations discussed in Section 6.2 as well as the expected false detection rate for the sample. Simulated sky realizations are filtered to match the real data, and noise realizations based on the measured map noise properties are added.

Each simulated sky is a Gaussian realization of the sum of the best-fit lensed *WMAP7*  $\Lambda$ CDM primary CMB model, a kSZ model, and point source contributions. The kSZ power spectrum is taken from the Sehgal et al. (2010) simulations and has an amplitude,  $D_l = l(l+1)C_l$ , of  $2.05 \mu\text{K}^2$  at  $\ell = 3000$ . We include both Poisson and clustered point sources. The Poisson contribution reflects both radio source and dusty, star-forming galaxy (DSFG) populations. The amplitude of the radio source term is set by the de Zotti et al. (2005) model source counts to an amplitude  $D_{3000}^r = 1.28 \mu\text{K}^2$  at 150 GHz with an assumed spectral index of  $\alpha_r = -0.6$  (defined by flux  $\propto \nu^\alpha$ ). The amplitude of the Poisson DSFG term at 150 GHz is  $D_{3000}^p = 7.7 \mu\text{K}^2$ . Finally, the clustered DSFG component is modeled by a  $D_\ell \propto \ell$  term normalized to  $D_{3000}^c = 5.9 \mu\text{K}^2$  at 150 GHz. The DSFG terms have an assumed spectral index of 3.6. The amplitude of each component was selected to be consistent with the Shirokoff et al. (2011) band powers.

For the determination of the SZ detection significance to cluster mass scaling, we also add a map of the tSZ effect; this tSZ map is not included when estimating the false detection rate. The tSZ map is drawn from a  $4000 \text{ deg}^2$  simulation by Shaw et al. (2010). Note that the limited sky area in this simulation means that we reuse the same tSZ maps between different fields in order to get 100 realizations. This limitation does not exist for the Gaussian realizations.

### 3.2. Expected False Detection Rates

We use the simulations described above, omitting the tSZ component, in order to estimate the rate of false detections arising from noise and non-cluster astrophysical signals. The resulting rates are shown in Figure 1. As expected, the false detection rate is essentially indistinguishable between the fields; there are the same number of  $N\sigma$  noise fluctuations per unit area.

The simulations lead to a prediction of 6.4 false detections in the  $>5\sigma$  catalog and 59 false detections in the  $>4.5\sigma$  catalog.

### 3.3. Integrated Comptonization

For each cluster candidate, we estimate the integrated Comptonization by fitting the cluster to a projected spherical  $\beta$ -model with  $\beta = 1$

$$Y(\theta) = y_0 \left(1 + \frac{\theta^2}{\theta_c^2}\right)^{-1}, \quad (3)$$

where  $y_0$  is peak Comptonization and  $\theta_c$  is the angular radius of the cluster core. The integrated Comptonization is defined as

$$Y_{\theta_l} = 2\pi \int_0^{\theta_l} Y(\theta) d\theta. \quad (4)$$

In Table 6, we set  $\theta_l = 1'$  and report  $Y_{1'}$ . We expect measurements of  $Y_{1'}$  to be robust despite the well known degeneracy between  $\theta_c$  and the central Compton parameter  $y_0$  for observations that do not resolve the cluster core (e.g., Planck Collaboration et al. 2011).

The likelihood of a set of cluster model parameters  $\mathcal{H}$  given our set of observed maps  $D_\nu(\bar{x})$  is defined as

$$\log(P(D|\mathcal{H})) = -\frac{1}{2} \sum_{\bar{k}, \nu_1, \nu_2} \frac{(\tilde{D}_{\nu_1}(\bar{k}) - \tilde{s}_{\nu_1}^{\mathcal{H}}(\bar{k}))(\tilde{D}_{\nu_2}(\bar{k}) - \tilde{s}_{\nu_2}^{\mathcal{H}}(\bar{k}))^*}{N_{\nu_1 \nu_2}(\bar{k})}, \quad (5)$$

where  $\tilde{D}_\nu(\bar{k})$  is the Fourier transform of the map for frequency  $\nu$ ,  $\tilde{s}_\nu^{\mathcal{H}}$  is the frequency-dependent Fourier transform of the cluster model for parameters set  $\mathcal{H}$  which we define as  $(\bar{x}, \theta_c, y_0)$ , and  $N_{\nu_1 \nu_2}(\bar{k})$  is the frequency-dependent covariance matrix of the set of maps which accounts for the same noise and astrophysical components used in the matched filter analysis. For the cluster profile, we use the projected spherical  $\beta$ -model defined above. We only fit the profile within  $\theta < 5\theta_c$ .

We use the Rapid Gridded Likelihood Evaluation (RGLE) method (T. Montroy et al., in preparation) to evaluate the cluster likelihood and compute  $Y_{1'}$ . The RGLE method is based on computing the likelihood for each cluster candidate on a fixed grid in parameter space. In this case, it is a four-dimensional grid over the parameters set  $\mathcal{H}$ . We define the extent of the grid as follows. The 2D position,  $\bar{x}$ , is constrained to be within 1.5 of the matched filter position. The central decrement is allowed to range from  $-4.3 \times 10^{-4}$  to  $2.2 \times 10^{-3}$ ; this prior does not impact the results. The core radius,  $\theta_c$ , is required to be between  $0'$  and  $7.5'$ . For cluster candidates at  $z > 0.125$ , we additionally limit the physical core radius ( $r_c$ ) of the cluster to be less than 1 Mpc. We translate between  $r_c$  and  $\theta_c$  based on the redshift of each cluster candidate (or redshift lower limit if unconfirmed). A core radius of 1 Mpc is much larger than the typical cluster size, so this limit allows full exploration of the likelihood degeneracy between  $Y_0$  and  $\theta_c$  while reducing the chance of bias due to noise fluctuations on scales much larger than the expected cluster size.

To compute the probability distribution for  $Y_{1'}$ , we first marginalize the four-dimensional grid over position (i.e.,  $\bar{x}$ ) to determine the two-dimensional likelihood surface for  $(\theta_c, y_0)$ . The value of  $Y_{1'}$  at each  $(\theta_c, Y_0)$  is calculated from Equation (4) with  $\theta_l = 1'$ . Formally, the likelihood for a given value of  $Y_{1'}$  can be computed by integrating the likelihood surface over curves

of constant  $Y_{1'}$ ,

$$P(D|Y_{1'} = Y_i) = \int dY_0 d\theta_c P(D|Y_0, \theta_c) \delta(Y_{1'}(Y_0, \theta_c) - Y_i). \quad (6)$$

The median value and 68% confidence intervals for  $Y_{1'}$  are determined from this likelihood function.

When applying the RGLE method to the SPT maps in order to estimate  $Y_{1'}$ , we use the calibration and beam shapes reported in Reichardt et al. (2012). We note that for the 2009 data, these are slightly different from the calibration and beam model described in Section 2.1 and used in cluster finding in this work. We use maps at 95 GHz (where available) and 150 GHz to estimate the cluster properties. To limit contamination from point sources, we use maps where previously identified point sources have been subtracted. The point source amplitudes are estimated using a variant of the RGLE which fits for the point source amplitudes given the beam shape. The point source subtraction significantly changes  $Y_{1'}$  for very few clusters since all affected point sources are at least  $8'$  away from any cluster candidate.

The RGLE method was previously used in Story et al. (2011) to compute integrated Comptonization for SPT follow-up observations of *Planck* ESZ cluster candidates (Planck Collaboration et al. 2011). The method has been verified by extensive simulations; we have also checked that the RGLE method produces comparable results to an alternative method based on Markov Chain Monte Carlo based sampling of the likelihood surface (B. Saliwanchik et al., in preparation).

## 4. EXTERNAL DATA

In this section, we briefly describe the optical, NIR, and X-ray data associated with this catalog. The optical/NIR follow-up strategy and analysis methods are summarized here and discussed in detail by S12. We also summarize the dedicated X-ray measurements of 14 SPT clusters, measurements which are used in the cosmological analysis here and which have been discussed in detail in previous SPT publications. Finally, we report X-ray fluxes and luminosities for all candidates that have identified counterparts in the *ROSAT* all-sky survey.

### 4.1. Optical and NIR Data

Every SPT-selected cluster candidate is followed up with optical imaging observations, and many candidates are also targeted with NIR imaging. Our strategy has evolved over time in order to utilize limited telescope resources to measure redshifts for the majority of cluster candidates. Briefly, the SPT candidates are pre-screened with Digitized Sky Survey (DSS) data. Candidates that appear to be at low redshift are followed up with the 1 m Swope telescope. Candidates that appear to be at high redshift (i.e., that do not appear in DSS images) are targeted with the 4 m Blanco telescope at CTIO or the 6.5 m Magellan telescopes at Las Campanas Observatory. The 4–6 m class observing is performed using an adaptive strategy, wherein candidates are imaged for a short time in three bands, then with a second pass in two bands if the cluster has not been detected. The second-pass imaging is designed to reach depths sufficient to confirm a  $z \sim 0.9$  cluster. Given weather and other constraints, not all candidates were observed to full depth.

Space-based NIR observations with *Spitzer*/IRAC were obtained at  $3.6 \mu\text{m}$  and  $4.5 \mu\text{m}$  for the subset of candidates that were both above a given significance threshold and not identified as low-redshift clusters in DSS data. The significance threshold was  $\xi \geq 4.5$  for 350 deg<sup>2</sup> of SPT coverage and  $\xi \geq 4.8$

for the remaining 370 deg<sup>2</sup> of SPT coverage. Candidates that were not imaged with *Spitzer*—and for which redshifts could not be estimated from the acquired optical data—were targeted with *K<sub>s</sub>*-band observations with the NEWFIRM camera on the Blanco 4 m.

A number of clusters were also observed using either long-slit or multi-slit spectrographs in subsequent follow-up projects. A robust biweight location estimator (Beers et al. 1990) is used to determine the cluster spectroscopic redshifts from ensemble spectra of member galaxies. Of the clusters in this work, 57 have spectroscopic redshifts, either from the literature or from our targeted observations. The redshifts are shown in Table 6, and the source for every spectroscopic redshift is presented by S12.

#### 4.2. Optical/NIR Imaging Data Reduction and Redshift Determination

All optical images are processed using the PHOTPIPE analysis pipeline (Rest et al. 2005; Miknaitis et al. 2007), as was done in previous SPT optical follow-up analyses (High et al. 2010; Williamson et al. 2011; Story et al. 2011). A separate reduction of the optical data from the Blanco Mosaic-II imager is performed using a version of the Dark Energy Survey (DES) data management pipeline (Mohr et al. 2008; Desai et al. 2012), which will eventually be used for analysis of data once the DES begins. The *Spitzer*/IRAC imaging data are processed from the standard online pipeline system and analyzed as described in Ashby et al. (2009); NEWFIRM data are reduced using the FATBOY pipeline (Eikenberry et al. 2006).

Redshifts are estimated for each candidate using three methods as described by S12. The first two methods are based on the identification of red-sequence overdensities and are described in detail in High et al. (2010) and Song et al. (2012a), respectively. The third method estimates photometric redshifts for individual galaxies using the ANNz algorithm (Collister & Lahav 2004), and cluster redshifts are estimated by measuring a peak in a manually selected red galaxy photometric redshift distribution. For a given cluster candidate, redshift estimates from the three methods are compared, outliers are flagged, and a combined redshift estimate is produced. In cases where only the *Spitzer*/IRAC 3.6 μm and 4.5 μm data are deep enough to detect the cluster, we use the High et al. (2010) method to estimate the redshift. Tests confirm this to be reliable at  $z > 0.7$  and a similar method is described in Stern et al. (2005) and Papovich (2008). These redshifts and associated uncertainties are shown in Table 6. If none of the three methods is successful at estimating a redshift for a given candidate, we report a lower redshift limit based upon the depth of the follow-up imaging.

#### 4.3. X-Ray Data

##### 4.3.1. Dedicated X-Ray Observations of SPT Clusters

As first reported in Andersson et al. (2011, hereafter A11), we have obtained *Chandra* and *XMM-Newton* data on 15 of the highest S/N clusters from the 2008 SPT survey fields, including 14 clusters in the redshift range used in the cosmological analysis in this work ( $z > 0.3$ ). B11 updated the X-ray observables for some clusters based on new spectroscopic redshifts (five clusters) or additional *Chandra* observations (five clusters). We refer the reader to A11 and B11 for additional details on these X-ray observations and the analysis of the associated data; the X-ray data here are identical to that used by B11.

From the X-ray data on this 14-cluster sample, density and temperature profiles were derived for use in our cosmological

analysis in Section 6. This was done by calculating  $T_X(r)$  and  $M_g(r)$  (allowing the calculation of  $Y_X(r)$  given a reference cosmology) from the X-ray observations of each cluster. Here  $r$  corresponds to a physical radius in the cluster,  $M_g(r)$  is the gas mass,  $T_X$  is the core-excised X-ray temperature, and  $Y_X$  is the product of  $M_g$  and  $T_X$ .

##### 4.3.2. ROSAT Counterparts

A number of cluster candidates are found to be associated with sources in the *ROSAT* Bright or Faint Source Catalog (Voges et al. 1999, 2000). For each of these, Table 1 lists intrinsic X-ray fluxes and rest-frame luminosities in the 0.5–2.0 keV band, inferred from the *ROSAT* count rates. The luminosities assume a reference cosmology chosen to match A11, who assumed a *WMAP7*+BAO+ $H_0$   $\Lambda$ CDM preferred cosmology with  $\Omega_M = 0.272$ ,  $\Omega_\Lambda = 0.728$  and  $H_0 = 70.2$  km s<sup>-1</sup> Mpc<sup>-1</sup> (Komatsu et al. 2011). The absorbing column density of Galactic hydrogen toward each cluster was accounted for using the H<sub>I</sub> survey of Kalberla et al. (2005), and the necessary redshift- and temperature-dependent *K*-corrections were performed using ICM temperature estimates based on the SPT signal to noise for each cluster for a simple power-law fit to the A11 data.<sup>35</sup>

These *ROSAT*-derived observables are reported only to provide further confirmation of these clusters; we emphasize that these results are *not* used in the cosmological analysis. Rather, only the X-ray observables from the 14-cluster *Chandra* and *XMM-Newton* data set from A11 and B11 are used in the cosmological analysis.

## 5. CLUSTER CATALOG

In Table 6, we present the complete list of galaxy cluster candidates from 720 deg<sup>2</sup> of sky surveyed by the SPT. The catalog includes 224 galaxy cluster candidates with detection significance,  $\xi \geq 4.5$ . Using optical/NIR follow-up data (see Section 4), we have determined redshifts for 158 of the SPT-selected galaxy cluster candidates. The median redshift of the sample is  $z = 0.55$ . The left panel of Figure 2 shows the redshift histogram of our cluster sample. The right panel shows SZ detection significance versus redshift for each cluster with an estimated redshift.

We search for galaxy clusters published in other catalogs within 2 arcmin of every candidate reported in Table 6 and within 5 arcmin of any candidate in Table 6 at  $z \leq 0.3$ . We query the SIMBAD<sup>36</sup> and NED<sup>37</sup> databases, and we manually search more recently published cluster catalogs such as the PLCKESZ (Planck Collaboration et al. 2011) and ACT-CL (Marriage et al. 2011) catalogs. All matches within the appropriate radius are listed in Table 2; whether the associations are physical or random superpositions is discussed in S12.

The optically confirmed, SZ-selected galaxy clusters are found to be massive, with a sharp mass cutoff at approximately  $M_{500} = 2.5 \times 10^{14} M_\odot h_{70}^{-1}$  at  $z = 0.6$ . We define  $M_{500}$  as the mass within a sphere of radius  $r_{500}$ , defined as the radius at which the density is 500 times the critical density. The exact mass cutoff depends on the field and cluster redshift. The

<sup>35</sup> We note, however, that the resulting flux and luminosity estimates are largely insensitive to the temperatures used. For example, adopting the temperature–luminosity relation of Mantz et al. (2010) results in luminosities that differ by  $\sim 2\% \pm 2\%$ , far less than the typical statistical uncertainty in the *ROSAT* count rates.

<sup>36</sup> <http://simbad.u-strasbg.fr/simbad>

<sup>37</sup> <http://nedwww.ipac.caltech.edu/>

**Table 1**  
*ROSAT* Counterparts

SPT ID	<i>ROSAT</i> ID	Offset ( $''$ )	$z$	<i>ROSAT</i> Counts ( $s^{-1}$ )	$F_X$ ( $10^{-13} \text{ erg cm}^{-2} \text{ s}^{-1}$ )	$L_X$ ( $10^{44} \text{ erg s}^{-1}$ )
SPT-CL J0233-5819	1RXS J023303.1-581939	13	0.6630	$0.0295 \pm 0.0131$	2.90	4.63
SPT-CL J0234-5831	1RXS J023443.1-583114	4	0.4150	$0.0800 \pm 0.0200$	7.95	4.12
SPT-CL J0254-5857	1RXS J025427.2-585736	80	0.4380	$0.0846 \pm 0.0305$	7.54	4.41
SPT-CL J0257-5842	1RXS J025744.7-584120	116	$0.43 \pm 0.03$	$0.0725 \pm 0.0298$	6.10	3.66
SPT-CL J0324-6236	1RXS J032412.7-623553	13	$0.72 \pm 0.04$	$0.0260 \pm 0.0121$	2.56	4.85
SPT-CL J0328-5541	1RXS J032833.5-554232	68	0.0844	$0.5700 \pm 0.0300$	47.28	1.31
SPT-CL J0333-5842	1RXS J033317.3-584244	38	$0.47 \pm 0.03$	$0.0125 \pm 0.0056$	1.13	0.82
SPT-CL J0337-6300	1RXS J033754.5-630122	49	$0.45 \pm 0.03$	$0.0166 \pm 0.0079$	1.78	1.22
SPT-CL J0343-5518	1RXS J034259.3-551905	58	$0.51 \pm 0.03$	$0.0167 \pm 0.0071$	1.35	1.21
SPT-CL J0354-5904	1RXS J035420.7-590545	92	$0.46 \pm 0.03$	$0.0105 \pm 0.0049$	0.91	0.62
SPT-CL J0402-6129	1RXS J040245.7-612939	32	$0.52 \pm 0.03$	$0.0082 \pm 0.0039$	0.74	0.70
SPT-CL J0403-5719	1RXS J040352.3-571936	10	$0.46 \pm 0.03$	$0.0391 \pm 0.0081$	3.06	2.11
SPT-CL J0404-6510	1RXS J040421.6-651004	72	$0.14 \pm 0.02$	$0.1300 \pm 0.0200$	13.55	0.74
SPT-CL J0410-6343	1RXS J041009.3-634319	43	$0.50 \pm 0.03$	$0.0291 \pm 0.0103$	2.88	2.44
SPT-CL J0411-6340	1RXS J041129.7-634133	47	$0.14 \pm 0.02$	$0.2600 \pm 0.0300$	25.83	1.26
SPT-CL J0412-5743	1RXS J041206.3-574313	3	$0.39 \pm 0.03$	$0.0231 \pm 0.0074$	1.85	0.88
SPT-CL J0423-5506	1RXS J042315.7-550710	58	$0.20 \pm 0.03$	$0.0332 \pm 0.0125$	2.24	0.25
SPT-CL J0431-6126	1RXS J043126.6-612622	40	0.0577	$0.9800 \pm 0.0700$	82.50	1.14
SPT-CL J0509-5342*	1RXS J050921.2-534159	18	0.4626	$0.0351 \pm 0.0118$	2.79	1.94
SPT-CL J0516-5430	1RXS J051634.0-543104	44	0.2950	$0.1200 \pm 0.0200$	10.86	2.71
SPT-CL J0521-5104	1RXS J052113.2-510419	37	0.6755	$0.0135 \pm 0.0062$	1.20	2.04
SPT-CL J0539-5744	1RXS J054010.1-574354	91	$0.76 \pm 0.03$	$0.0123 \pm 0.0053$	1.47	3.32
SPT-CL J0546-5345*	1RXS J054638.7-534434	69	1.0670	$0.0123 \pm 0.0044$	1.59	7.55
SPT-CL J0551-5709*	1RXS J055126.4-570843	91	0.4230	$0.0271 \pm 0.0053$	3.41	1.96
SPT-CL J0559-5249*	1RXS J055942.1-524950	15	0.6112	$0.0109 \pm 0.0042$	1.29	1.65
SPT-CL J2011-5725	1RXS J201127.9-572507	28	0.2786	$0.1100 \pm 0.0300$	12.25	2.80
SPT-CL J2012-5649	1RXS J201238.3-565038	103	0.0552	$1.1400 \pm 0.0900$	130.40	0.96
SPT-CL J2016-4954	1RXS J201603.5-495530	47	$0.26 \pm 0.03$	$0.0273 \pm 0.0127$	2.98	0.59
SPT-CL J2018-4528	1RXS J201828.7-452720	95	$0.41 \pm 0.03$	$0.0298 \pm 0.0129$	2.97	1.62
SPT-CL J2021-5256	1RXS J202155.7-525721	52	$0.11 \pm 0.02$	$0.0600 \pm 0.0200$	6.62	0.20
SPT-CL J2023-5535	1RXS J202321.2-553534	9	0.2320	$0.0900 \pm 0.0200$	10.58	1.54
SPT-CL J2025-5117	1RXS J202554.4-511647	41	$0.18 \pm 0.02$	$0.0500 \pm 0.0100$	5.12	0.43
SPT-CL J2032-5627	1RXS J203215.2-562753	47	0.2840	$0.0542 \pm 0.0180$	6.64	1.54
SPT-CL J2121-6335	1RXS J212157.9-633459	103	$0.23 \pm 0.03$	$0.1000 \pm 0.0200$	9.85	1.48
SPT-CL J2130-6458	1RXS J213056.1-645909	36	0.3160	$0.0437 \pm 0.0189$	4.33	1.28
SPT-CL J2136-4704	1RXS J213624.5-470453	38	0.4250	$0.0286 \pm 0.0114$	2.58	1.50
SPT-CL J2138-6007	1RXS J213801.2-600801	5	0.3190	$0.0750 \pm 0.0211$	7.74	2.26
SPT-CL J2145-5644	1RXS J214559.3-564455	55	0.4800	$0.0413 \pm 0.0162$	4.01	2.91
SPT-CL J2146-5736	1RXS J214643.9-573723	43	$0.60 \pm 0.03$	$0.0277 \pm 0.0119$	2.64	3.36
SPT-CL J2201-5956	1RXS J220157.8-595648	33	0.0983	$1.0800 \pm 0.0400$	108.10	2.57
SPT-CL J2259-5432	1RXS J225957.0-543118	51	$0.44 \pm 0.04$	$0.0225 \pm 0.0098$	1.68	1.07
SPT-CL J2259-5617	1RXS J230001.2-561709	17	$0.17 \pm 0.02$	$0.1400 \pm 0.0200$	11.29	0.87
SPT-CL J2300-5331	1RXS J230039.8-533118	28	0.2620	$0.0800 \pm 0.0200$	5.81	1.16
SPT-CL J2332-5358*	1RXS J233224.3-535840	17	0.4020	$0.1600 \pm 0.0300$	12.29	6.23
SPT-CL J2337-5942*	1RXS J233726.6-594205	18	0.7750	$0.0271 \pm 0.0136$	2.18	4.64

**Notes.** Cluster candidates coincident with sources in the *ROSAT* bright or faint source catalogs (Voges et al. 1999, 2000). We define a match if a candidate is within  $5'$  of a cluster candidate at  $z \leq 0.3$  or within  $2'$  of a candidate at  $z > 0.3$ . For each source, we estimate the X-ray luminosity and flux based on the measured redshift, position on the sky, and *ROSAT* X-ray photon counts. Clusters marked with a “\*” also have  $Y_X$  estimates from *XMM* or *Chandra* presented by A11 and B11. Note that SPT-CL J0311-6354 is coincident with IES0310-64.0, but not a *ROSAT* source. We also quote the cluster redshift used in this work (see Section 4). We include error bars for red-sequence redshifts, but not spectroscopic redshifts.

mass cutoff is the product of two things: (1) the probability to detect a cluster which falls exponentially toward lower masses and (2) the true cluster mass distribution which naturally rises sharply toward lower masses. The chance to detect an individual cluster at the mass cutoff is fairly low. We discuss mass estimates for the clusters in Section 7.1.2, and we show the estimated masses versus redshift in Figure 3. The most massive cluster is SPT-CL J2106-5844 at  $z = 1.1320$  with a mass of  $M_{500} = 8.39 \pm 1.68 \times 10^{14} M_{\odot} h_{70}^{-1}$ . This is the most massive cluster at  $z > 1$  currently known. Foley et al. (2011) showed that although this cluster is rare, it is not in significant tension with

the  $\Lambda$ CDM model. The least massive is SPT-CL J2007-4906 at  $z = 1.25 \pm 0.11$  with  $M_{500} = 2.11 \pm 0.82 \times 10^{14} M_{\odot} h_{70}^{-1}$ . The median mass of the sample is  $3.3 \times 10^{14} M_{\odot} h_{70}^{-1}$ .

We compare the mass and redshift distribution of this SPT cluster catalog to cluster catalogs from the *ROSAT* and *Planck* all-sky surveys in Figure 4. For the *ROSAT* all-sky survey, we show 917 clusters taken from the NORAS, REFLEX, and MACS cluster catalogs, as given in the MCXC compilation (Piffaretti et al. 2011). We use the redshift and mass estimates reported by Piffaretti et al. (2011), where the masses were estimated from the X-ray luminosity–mass relation. We also

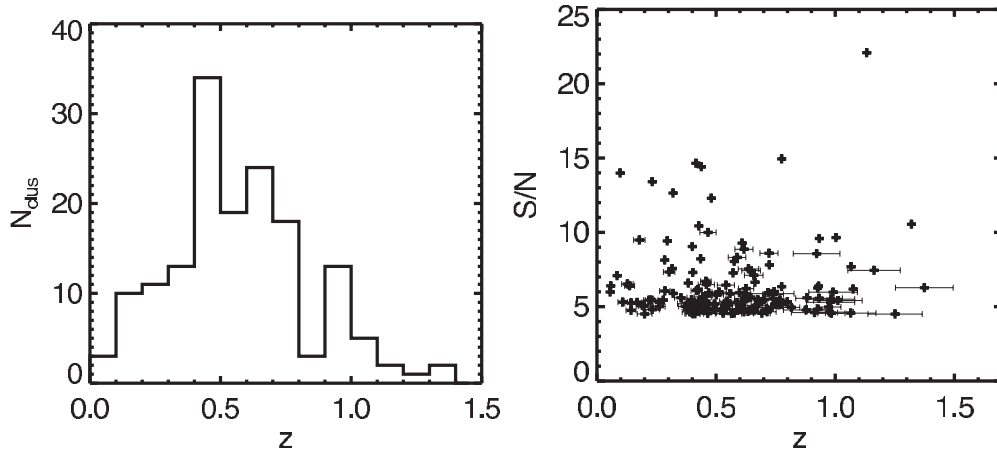


**Figure 2.** Left panel: redshift histogram for the optically confirmed,  $\xi > 4.5$  galaxy clusters in this sample. The median redshift of the sample is 0.55. The median redshift of the sample used in the cosmological analysis ( $z > 0.3$  and  $\xi > 5$ ) is 0.62. Right panel: detection significance vs. redshift for all optically confirmed galaxy clusters in this sample.

**Table 2**  
Clusters with Matches in Other Catalogs

SPT ID	First ID, Ref.	All Catalogs with Match	$z$	Lit. $z$ , Ref.
SPT-CL J0254-5857	SPT-CL J0254-5856, A	A,B	0.4380	0.4380, A
SPT-CL J0328-5541	ACO 3126, C	B,C,D,E,F,G	0.0844	0.0844, H
SPT-CL J0404-6510	ACO 3216, C	C	$0.14 \pm 0.02$	0.14, I
SPT-CL J0411-6340	ACO 3230, C	C	$0.14 \pm 0.02$	0.14, I
SPT-CL J0431-6126	Ser 40-6, J	B,C,D,E,F,G,J,K	0.0577	0.0577, H
SPT-CL J0458-5741	ACO 3298, C	C	Unconfirmed	...
SPT-CL J0509-5342	SPT-CL 0509-5342, L	L,M,N	0.4626	0.4626, O
SPT-CL J0511-5154	SCSO J051145-515430, P	M,P	0.6450	0.74, O
SPT-CL J0516-5430	ACO S 0520, C	B,C,G,L,M,N,P	0.2950	0.2950, G
SPT-CL J0521-5104	SCSO J052113-510418, P	M,P	0.6755	0.6755, Q
SPT-CL J0522-5026	SCSO J052200-502700, P	P	$0.53 \pm 0.04$	0.50, P
SPT-CL J0528-5300	SPT-CL 0528-5300, L	L,M,N,P	0.7648	0.7648, O
SPT-CL J0546-5345	SPT-CL 0547-5345, L	L,M,N	1.0670	1.0670, R
SPT-CL J0559-5249	SPT-CL J0559-5249, M	M,N	0.6112	0.6112, O
SPT-CL J2011-5725	RXC J2011.3-5725, G	G	0.2786	0.2786, G
SPT-CL J2012-5649	Str 2008-569, K	B,C,E,G,K,S	0.0552	0.0552, H
SPT-CL J2020-4646	ACO 3673, C	C	$0.19 \pm 0.02$	...
SPT-CL J2021-5256	Ser 138-5, J	C,G,J	$0.11 \pm 0.02$	...
SPT-CL J2023-5535	RXC J2023.4-5535, G	A,B,G	0.2320	0.2320, G
SPT-CL J2025-5117	ACO S 0871, C	C	$0.18 \pm 0.02$	...
SPT-CL J2032-5627	CIG 2028.3-5637, T	C,G,T	0.2840	0.0608, H
SPT-CL J2055-5456	ACO 3718, C	C,G	$0.13 \pm 0.02$	...
SPT-CL J2059-5018	ACO S 0912, C	C	$0.41 \pm 0.03$	...
SPT-CL J2101-5542	ACO 3732, C	C	$0.20 \pm 0.02$	...
SPT-CL J2121-6335	ACO S 0937, C	C	$0.23 \pm 0.03$	...
SPT-CL J2201-5956	CIG 2158.3-6011, T	A,B,C,D,E,F,G,T	0.0972	0.0972, H
SPT-CL J2259-5617	ACO 3950, C	C,M	$0.17 \pm 0.02$	...
SPT-CL J2300-5331	ACO S 1079, C	C,M	0.2620	0.29, O
SPT-CL J2332-5358	SCSO J233227-535827, P	M,P	0.4020	0.32, U
SPT-CL J2351-5452	SCSO J235138-545253, P	P	0.3838	0.3838, V

**Notes.** Cluster candidates coincident with galaxy clusters identified in other catalogs. We define a match if a candidate is within  $5'$  ( $2'$ ) of an identified cluster for clusters at  $z < 0.3$  ( $z > 0.3$  or unconfirmed). For each match, we report the name under which the cluster was first reported and all catalogs which include the cluster. See S12 for a discussion of physical association versus random superposition for these matches. We also quote the cluster redshift used in this work—either the photometric redshift estimated in S12 or a spectroscopic redshift obtained from follow-up observations or the literature. We include error bars for red-sequence redshifts but not spectroscopic redshifts. In the last column, we quote a redshift from the literature if available. Error bars are not reported for literature redshifts; two (four) significant digits are used if the literature redshift is photometric (spectroscopic). A: SPT-CL catalog (W11); B: PLCKESZ catalog (Planck Collaboration et al. 2011); C: ACO catalog (Abell et al. 1989); D: APMCC catalog (Dalton et al. 1997); E: [DBG99] catalog (de Grandi et al. 1999); F: [DEM94] catalog (Dalton et al. 1994); G: REFLEX catalog (Böhringer et al. 2004); H: Struble & Rood (1999); I: Ebeling et al. (1996); J: Sersic catalog (Sérsic 1974); K: Stromlo catalog (Duus & Newell 1977); L: SPT-CL catalog (Staniszewski et al. 2009); M: SPT-CL catalog (V10); N: ACT-CL catalog (Marriage et al. 2011); O: H10; P: SCSO catalog (Menanteau et al. 2010); Q: Sifon et al. (2012); R: Brodwin et al. (2010); S: [QW] catalog (Quintana & White 1990); T: CIG catalog (Fetisova 1981); U: Šuhada et al. (2010); V: Buckley-Geer et al. (2011).



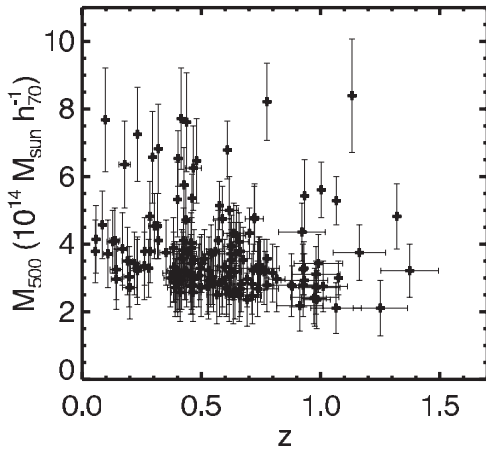


**Figure 3.** Cluster mass estimates vs. redshift for all optically confirmed galaxy clusters in this sample. The reported mass has been deboosted and marginalized over the allowed set of cosmological and scaling relation parameters for a  $\Lambda$ CDM cosmology.

show the 155 out of 189 galaxy clusters in the *Planck*-ESZ cluster catalog (Planck Collaboration et al. 2011) that have counterparts in the MCXC compilation. The plotted masses and redshifts for these clusters are taken from the MCXC compilation. The mass estimates for the SPT clusters are described in Section 7.1.2. The selection function of the SPT catalog is nearly independent of redshift. In fact, the minimum mass drops slightly with redshift as the angular size of galaxy clusters decreases, becoming better matched to the SPT beam and less confused by primary CMB fluctuations. This reduction in size with increasing redshift has the opposite effect on the *Planck* SZ survey due to the *Planck* satellite’s larger beam size ( $7'$  at 143 GHz). Beam dilution reduces the *Planck* satellite’s S/N on high-redshift clusters, while the outstanding frequency coverage makes it possible to subtract the primary CMB on large angular scales and recover the SZ signal from low-redshift galaxy clusters. Finally, the *ROSAT* cluster mass threshold rises with redshift due to cosmological dimming of the X-ray flux, crossing over the SPT selection function around  $z \sim 0.3$ .

The catalog presented here is expected to be 95% pure for detection significance  $\xi \geq 5$  and 71% pure for detection significance  $\xi \geq 4.5$ . This agrees well with the actual optical and NIR confirmation rate. From Section 3.2, we expect 59 (6.4) candidates to be false above a detection significance of 4.5 (5). We find that 66 (6) candidates do not have optical counterparts, which is in excellent agreement with the expected number of false detections.

### 5.1. Cluster Candidates in the Point-source-masked Regions

As discussed in Section 3, any cluster detections within  $8'$  of an emissive point source detected above  $5\sigma$  at 150 GHz are rejected. We do this because residual source flux or artifacts due to the masking of these point sources can cause spurious decrements when the maps are filtered. A total area of  $\sim 50$  out of  $770 \text{ deg}^2$  ( $\sim 6.5\%$ ) was excluded from cluster finding for this reason. This conservative procedure is appropriate for constructing a cluster catalog with a clean, easy-to-define selection function and a mass-observable relation with minimal outliers. However, it is likely that several massive clusters will lie within the exclusion region, and some of those clusters might be only minimally affected by the nearby emissive source. If we assume no spatial correlation between sources and clusters, we would expect roughly eight missed clusters above  $\xi = 5$ .

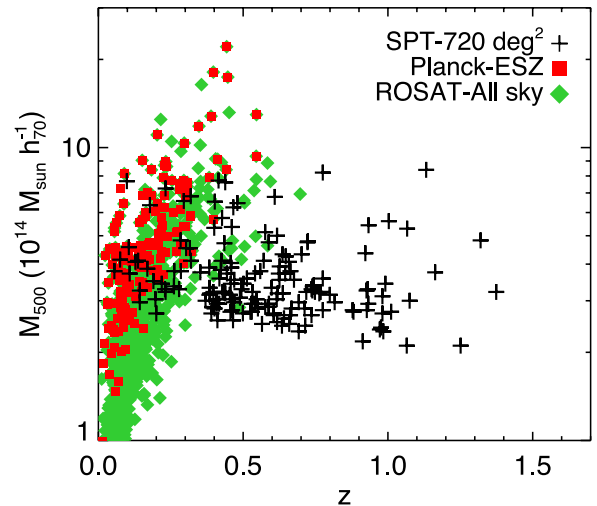


**Figure 4.** Mass estimates vs. redshift for three cluster samples: (1) optically confirmed SZ-selected galaxy clusters from the SPT survey, (2) SZ-selected galaxy clusters from the *Planck* survey (Planck Collaboration et al. 2011), and (3) X-ray-selected galaxy clusters from the *ROSAT* all-sky survey (Piffaretti et al. 2011). High-resolution SZ surveys, such as that performed with the SPT, uniquely have a nearly redshift independent selection function. The redshift-dependent selection in the *Planck* survey is due to beam dilution; the redshift dependence of the *ROSAT* catalog is due to cosmological dimming.

(A color version of this figure is available in the online journal.)

**Table 3**  
Cluster Candidates Above  $\xi = 5$  in the Source-masked Area

SPT ID	R.A.	Decl.	$\xi$	$\theta_c$
SPT-CL J0334-6008	53.7116	-60.1541	6.97	1.25
SPT-CL J0434-5727	68.6517	-57.4568	5.07	0.75
SPT-CL J0442-5905	70.6707	-59.0975	6.42	0.25
SPT-CL J2142-6419	325.7280	-64.3268	11.01	0.25
SPT-CL J2154-5952	328.7210	-59.8878	7.16	0.50
SPT-CL J2154-5936	328.7230	-59.6121	6.28	0.50

**Notes.** Cluster candidates identified in a non-standard cluster-finding analysis in which only the very brightest ( $> 100 \text{ mJy}$ ) point sources are masked (see the text for details). Only candidates from the area masked in the standard analysis are listed here. These candidates are not included in the cosmological analysis or in the total number of candidates quoted in the text.

As in W11, we re-ran the cluster-finding algorithm on all the fields used in this work with only the very brightest sources masked. For this work we used a bright-source threshold of  $S_{150\text{GHz}} > 100 \text{ mJy}$ , compared to the normal threshold of  $\sim 6 \text{ mJy}$ , resulting in a total masked area of  $< 3 \text{ deg}^2$ . Each detection with  $\xi \geq 5$  from the originally masked area was visually inspected (below the  $\xi = 5$  threshold, it becomes too difficult to distinguish visually between real clusters and artifacts), and the vast majority were rejected as obvious point-source-related artifacts. Some detections, however, did appear to be significant SZ decrements only minimally affected by the nearby source. These objects are listed in Table 3. We find six objects above  $\xi = 5$ , consistent within Poisson uncertainties with the expected number. One of these objects, SPT-CL J2142-6419, was also identified in the auxiliary detection procedure in W11. Two of the six objects (SPT-CL J2154-5952 and SPT-CL J2154-5936) are unusually close to one another on the sky ( $16'.5$  separation), but visual inspection shows nothing out of the ordinary about either candidate beyond its proximity to an emissive source.

We have not yet attempted to obtain redshifts for these six cluster candidates, and they are not included in the cosmological analysis or in the total number of candidates quoted in the rest of the text. We perform the same search for counterparts to these six candidates in other galaxy cluster catalogs as we do for the main sample. We find no galaxy cluster matches, though we do find X-ray sources within 5 arcmin of SPT-CL J0334-6008 and within 2 arcmin of SPT-CL J0434-5727, SPT-CL J0442-5905, and SPT-CL J2154-5936.

## 6. COSMOLOGICAL MODELING

In this section, we briefly review the method presented by B11 to use the combination of an SZ-selected cluster catalog and X-ray follow-up observations to investigate cosmological constraints; we refer the reader to B11 for a complete description. We also present a slightly modified algorithm to treat fields of varying depths.

We use Monte Carlo Markov chain (MCMC) methods to determine parameter constraints. As outlined by B11, we have extended CosmoMC<sup>38</sup> (Lewis & Bridle 2002) to simultaneously fit the SZ and X-ray cluster observable-mass relations while also varying cosmological parameters. We include all  $\xi > 5$  and  $z > 0.3$  cluster candidates in this catalog (100 clusters) in the cosmological analysis as well as the X-ray observations of 14 SPT-selected clusters described by A11 and B11. These data will be referred to as SPT<sub>CL</sub>.

In addition to the cluster data, some MCMCs include CMB data from WMAP7 and SPT (Komatsu et al. 2011; Keisler et al. 2011). In some cases, we also add measurements of the BAO feature using SDSS and 2dFGRS data (Percival et al. 2010), low-redshift measurements of  $H_0$  from the *Hubble Space Telescope* (Riess et al. 2011), or measurements of the luminosity–distance relationship from the Union2 compilation of 557 SNe (Amanullah et al. 2010). Finally, we sometimes use a BBN prior on the baryon density from measurements of the abundances of deuterium (Kirkman et al. 2003). In all cases, we set the helium abundance based on the predictions of BBN (Hamann et al. 2008).

### 6.1. X-Ray Scaling Relations

Following Vikhlinin et al. (2009b) and B11, we use  $Y_X$  as an X-ray proxy for cluster mass,  $M_{500}$ . We assume a  $Y_X - M_{500}$  relation of the form

$$\frac{M_{500}}{10^{14} M_{\odot} h^{-1}} = (A_X h^{3/2}) \left( \frac{Y_X}{3 \times 10^{14} M_{\odot} \text{keV}} \right)^{B_X} \left( \frac{H(z)}{H_0} \right)^{C_X}, \quad (7)$$

parameterized by the normalization  $A_X$ , the slope  $B_X$ , the redshift evolution  $C_X$ , and a log-normal scatter  $D_X$  on  $Y_X$ . We express the mass in units of  $M_{\odot} h^{-1}$  to match the  $\zeta - M_{500}$  relation in Section 6.2. For our cosmological analysis, we assume the same Gaussian priors on the scaling relation parameters as B11. The priors are motivated by constraints from X-ray measurements by Vikhlinin et al. (2009a) and simulations, and are discussed in detail by B11. The Gaussian priors are  $A_X = 5.77 \pm 0.56$ ,  $B_X = 0.57 \pm 0.03$ ,  $C_X = -0.4 \pm 0.2$ , and  $D_X = 0.12 \pm 0.08$ . We do not see movement away from these priors (i.e., evidence for tension between the prior and data) in the MCMCs presented in later sections. The scaling relation has more freedom than required by the data; if all parameters except  $A_X$  are fixed, the cosmological results are unchanged.

### 6.2. SZ Scaling Relations

As in V10 and B11, we estimate galaxy cluster masses according to an SZ S/N to mass scaling relation. Following those works, we introduce the unbiased significance,  $\zeta$ , since the relation between  $\xi$  and halo mass is complicated by the comparable effects of intrinsic scatter and instrumental noise. The unbiased significance is defined to be the average detection S/N of a simulated cluster, measured across many noise realizations, and related to the detection significance  $\xi$  as follows:

$$\zeta = \sqrt{\langle \xi \rangle^2 - 3} \quad (8)$$

at  $\xi > 2$ . The detection significance  $\xi$  is maximized across possible cluster positions and filters scales, effectively adding three degrees of freedom to the fit. The unbiased significance  $\zeta$  removes this maximization bias.

The specific form of the scaling relation is

$$\zeta = A_{SZ} \left( \frac{M_{500}}{3 \times 10^{14} M_{\odot} h^{-1}} \right)^{B_{SZ}} \left( \frac{H(z)}{H(0.6)} \right)^{C_{SZ}}, \quad (9)$$

where  $A_{SZ}$  is a normalization,  $B_{SZ}$  a mass evolution, and  $C_{SZ}$  a redshift evolution. The method to go from simulations to an SZ S/N to mass scaling relation is described in more detail by V10.

As described more fully in V10, this scaling relation is based on SZ simulations of approximately 4000 deg<sup>2</sup> of sky. The simulations used in this work are described in Section 3.1. The intrinsic scatter,  $D_{SZ}$ , was measured to be 24% in these simulations. The main uncertainty for cosmological purposes is on the mass normalization,  $A_{SZ}$ , which is assumed to be uncertain at the 30% level (V10).

Note that the dusty galaxies, radio galaxies and the kSZ effect in these simulations are not correlated with the tSZ effect. B11 argue that the level of correlated emission from dusty or radio galaxies is negligible; these arguments apply equally well to this sample since the mass and redshift ranges are similar. The probability of a chance superposition from a bright point source ( $\gtrsim 6$  mJy) is negligible given the sky density of sources ( $\sim 1$  deg<sup>-2</sup>; Vieira et al. 2010). We have tested whether including the correlation between the kSZ and tSZ signals would impact the predicted scaling relation. We find only small changes to  $A_{SZ}$ ,  $< 3\%$  which is less than  $0.1\sigma$  for the prior. There is also a small increase in the scatter of less than  $0.2\sigma$  of the prior width. As these corrections are tiny compared to the overall prior uncertainties, we do not include them in this analysis.

Unlike V10, this analysis includes fields with substantially different noise levels. We have repeated the simulations (see Section 3.1) on each field, and find the main effect is an overall rescaling of the expected SZ S/N for a given cluster mass, i.e., a change to  $A_{SZ}$ . There is a slight change to the redshift evolution between fields as well, but neglecting this results in an additional percent level scatter which is completely negligible given the overall 24% scatter in the scaling relation. We have also checked the simulations by adding known cluster profiles to the real maps, applying the cluster-finding algorithm and checking the recovered S/N. This semi-analytic test agrees well with the results of the simulations. We apply a fixed rescaling of  $A_{SZ}$  to each field, as tabulated in Table 4. The normalization of the rescaling is chosen such that the RA5H30DEC-55 field is unity. We use simulations of all five fields to estimate the parameters  $A_{SZ}$ ,  $B_{SZ}$ ,  $C_{SZ}$ , and  $D_{SZ}$  for the combined scaling relation, and determine values of 6.24, 1.33, 0.83, and 0.24 respectively. Uncertainties in the SZ modeling lead to significant

<sup>38</sup> <http://cosmologist.info/cosmomc/>

**Table 4**  
SZ Mass Normalization per Field

Name	Year	Scaling Factor
RA5H30DEC-55	2008	1.00
RA23H30DEC-55	2008	1.01
RA3H30DEC-60	2009	1.25
RA21HDEC-50	2009	1.09
RA21HDEC-60	2009	1.31

**Notes.** The estimated scaling factors for the mass normalization  $A_{SZ}$  for each field. These factors correct for the different noise levels in each field.

systematic uncertainties on these scaling relation parameters. Following V10, we apply conservative 1.872, 0.266, 0.415, and 0.048 (30%, 20%, 50%, and 20%) Gaussian uncertainties to  $A_{SZ}$ ,  $B_{SZ}$ ,  $C_{SZ}$ , and  $D_{SZ}$ , respectively.

### 6.3. Cluster Likelihood Function

We have written a module extension to CosmoMC to calculate the cluster likelihood function. In essence, this module uses the Cash statistic (Cash 1979) to compare the observed number counts to a known Poisson distribution at each step in the MCMC. The method closely mirrors that presented by B11, to whom we refer the reader for a complete description. Briefly, we use the Tinker mass function (Tinker et al. 2008) to calculate the mass function based on the cosmological parameters and associated matter power spectra estimated by CAMB (Lewis et al. 2000) at 20 logarithmically spaced redshifts between  $0 < z < 2.5$ . The mass function is calculated for an overdensity of 500 times the critical density. Using the scaling relation parameters at that step of the MCMC, the mass function is translated from the native  $M_{500-z}$  space into the three-dimensional observable space, with axes corresponding to the SZ detection significance  $\xi$ , the X-ray parameter  $Y_X$ , and the optically derived redshift  $z$ . The observed number counts are compared to the expectation values in this three dimensional space to evaluate the likelihood for that step of the MCMC.

There are two differences between the likelihood function used in this work and that presented by B11. The most significant of these is the field-dependent SZ scaling relation described in Section 6.2. In practice, this means that the above calculation is done separately for each of the five fields, and the resulting log likelihoods are summed.

The treatment of unconfirmed cluster candidates is the second, more minor difference between this work and B11. B11 left unconfirmed clusters out of the analysis; this is appropriate given the extremely high redshift lower limit on the single unconfirmed (and almost certainly false) cluster candidate in that cluster sample. A more rigorous treatment includes the like-

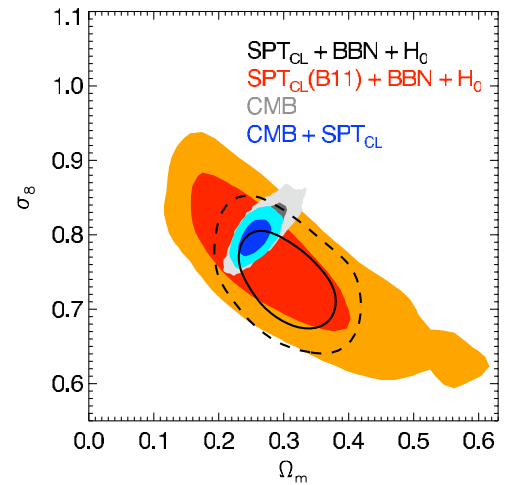


**Figure 5.** 68% and 95% likelihood contours in the  $\Omega_m$ - $\sigma_8$  plane for different data sets. The additional clusters in this catalog reduce the allowed parameter volume by a factor of two compared to B11 when considering the SPT<sub>CL</sub>+BBN+ $H_0$  data. However, the linear combination showing the most improvement is already well constrained by the CMB data. Therefore as predicted by B11, the additional clusters will not substantially improve constraints for the CMB+SPT<sub>CL</sub> data until the mass calibration is improved.

likelihood of each unconfirmed candidate, using the expectation value of the candidate being either a higher redshift cluster or a false detection. This expectation value is the sum of the expected number of false detections at a given detection significance and a redshift-dependent selection function convolved by the mass function. In practice, the treatment of unconfirmed clusters is nearly negligible since the  $S/N > 5$  sample used to derive cosmological constraints has high purity and the precision of the cosmological constraints is currently limited by the systematic mass calibration uncertainty.

With this in mind, we make two simplifying approximations in our implementation. First, we neglect any cosmological dependence in the false detection rate—the simulations used to calculate the false detection rate are only run for one cosmological model. This effect should be negligible since the CMB and foreground power levels are well-known. Second, we treat the redshift selection function for unconfirmed candidates as a Heaviside function at the quoted redshift limit for that cluster candidate. The chance of detecting a cluster out to this redshift is nearly unity with the current optical and NIR observations. We have tested shifting the Heaviside function to  $z > 1.5$  or  $z > 2$  and find no impact on the cosmological constraints. This can be understood intuitively because (1) the overall purity is high, and (2) the expected number of unconfirmed, real,

**Table 5**  
Cosmological Constraints

	$\Lambda$ CDM		wCDM		$\sum m_\nu$	
	CMB	+SPT <sub>CL</sub>	CMB + BAO + $H_0$ + SNe	+ SPT <sub>CL</sub>	CMB + BAO + $H_0$	+ SPT <sub>CL</sub>
$\Omega_c h^2$	$0.1109 \pm 0.0048$	$0.1086 \pm 0.0031$	$0.1140 \pm 0.0041$	$0.1104 \pm 0.0029$	$0.1113 \pm 0.0030$	$0.1113 \pm 0.0025$
$\sigma_8$	$0.808 \pm 0.024$	$0.798 \pm 0.017$	$0.840 \pm 0.038$	$0.807 \pm 0.027$	$0.775 \pm 0.041$	$0.766 \pm 0.028$
$\Omega_m$	$0.267 \pm 0.026$	$0.255 \pm 0.016$	$0.269 \pm 0.014$	$0.262 \pm 0.013$	$0.274 \pm 0.016$	$0.275 \pm 0.015$
$H_0$	$70.71 \pm 2.17$	$71.62 \pm 1.53$	$71.20 \pm 1.49$	$71.15 \pm 1.51$	$69.83 \pm 1.36$	$69.76 \pm 1.31$
$w$			$-1.054 \pm 0.073$	$-1.010 \pm 0.058$		
$\sum m_\nu$ (95% CL)					$<0.44$	$<0.38$

**Note.** Cosmological constraints for three models with and without the SPT cluster sample.

**Table 6**  
Galaxy Clusters Above  $4.5\sigma$  in  $720 \text{ deg}^2$  Observed by the SPT

ID and Coordinates			$Y_{SZ} \times 10^6$	Significances			Best		Redshift	$M_{500}$
SPT ID	R.A.	Decl.	(arcmin $^2$ )	$\theta_c = 0'.5$	$1'.5$	$2'.5$	$\xi$	$\theta_c$		( $10^{14} h_{70}^{-1} M_{\odot}$ )
SPT-CLJ0000-5748*	0.2496	-57.8066	107 ± 24	5.48	4.84	4.38	5.48	0.50	0.7019	4.29 ± 0.71
SPT-CLJ0201-6051	30.3933	-60.8592	73 ± 19	4.44	3.50	2.39	4.83	0.25	>1.05 <sup>a</sup>	...
SPT-CLJ0203-5651	30.8309	-56.8612	74 ± 19	4.78	4.02	2.45	4.98	0.25	>1.00 <sup>a</sup>	...
SPT-CLJ0205-5829	31.4437	-58.4856	185 ± 19	10.39	8.96	7.19	10.54	0.25	1.3220	4.79 ± 1.00
SPT-CLJ0205-6432	31.2786	-64.5461	103 ± 19	6.02	5.04	3.91	6.02	0.50	0.7440	3.29 ± 0.79
SPT-CLJ0209-5452	32.3491	-54.8794	83 ± 21	4.52	4.40	4.05	4.52	0.50	0.42 ± 0.03	2.46 ± 0.89
SPT-CLJ0211-5712	32.8232	-57.2157	66 ± 21	4.65	3.66	3.05	4.77	0.25	>1.03 <sup>a</sup>	...
SPT-CLJ0216-5730	34.1363	-57.5100	85 ± 20	4.72	4.48	3.79	4.72	0.50	>1.03 <sup>a</sup>	...
SPT-CLJ0216-6409	34.1723	-64.1562	94 ± 19	5.53	4.92	4.27	5.54	0.25	0.64 ± 0.03	3.07 ± 0.86
SPT-CLJ0218-5826	34.6251	-58.4386	78 ± 20	4.48	4.15	3.17	4.54	0.25	0.57 ± 0.03	2.36 ± 0.86
SPT-CLJ0221-6212	35.4382	-62.2044	65 ± 19	4.53	3.66	2.96	4.71	0.25	>1.20 <sup>a</sup>	...
SPT-CLJ0230-6028	37.6410	-60.4694	98 ± 19	5.79	4.87	3.84	5.88	0.25	0.74 ± 0.08	3.21 ± 0.79
SPT-CLJ0233-5819	38.2561	-58.3269	131 ± 20	6.34	6.44	5.67	6.64	1.25	0.6630	3.71 ± 0.86
SPT-CLJ0234-5831	38.6790	-58.5217	270 ± 19	14.65	13.03	10.54	14.65	0.50	0.4150	7.64 ± 1.50
SPT-CLJ0239-6148	39.9120	-61.8032	74 ± 19	4.50	3.46	2.75	4.67	0.25	>1.06 <sup>a</sup>	...
SPT-CLJ0240-5946	40.1620	-59.7703	169 ± 19	8.99	8.64	7.63	9.04	0.75	0.4000	5.29 ± 1.07
SPT-CLJ0240-5952	40.1982	-59.8785	74 ± 19	4.53	3.64	2.50	4.65	0.25	0.62 ± 0.03	2.43 ± 0.86
SPT-CLJ0242-6039	40.6551	-60.6526	90 ± 20	4.87	4.77	4.26	4.92	1.00	>1.50 <sup>a</sup>	...
SPT-CLJ0243-5930	40.8616	-59.5132	126 ± 19	7.30	6.23	5.18	7.42	0.25	0.65 ± 0.03	4.18 ± 0.89
SPT-CLJ0249-5658	42.4068	-56.9764	96 ± 20	5.37	5.21	4.48	5.44	0.75	0.23 ± 0.02	3.32 ± 0.89
SPT-CLJ0253-6046	43.4605	-60.7744	86 ± 21	4.61	4.73	4.27	4.83	1.25	0.44 ± 0.02	2.71 ± 0.86
SPT-CLJ0254-5857	43.5729	-58.9526	295 ± 22	13.61	14.42	13.82	14.42	1.50	0.4380	7.46 ± 1.46
SPT-CLJ0254-6051	43.6015	-60.8643	127 ± 21	6.35	6.59	5.75	6.71	1.00	0.44 ± 0.02	4.00 ± 0.93
SPT-CLJ0256-5617	44.1009	-56.2973	136 ± 19	7.54	6.98	5.83	7.54	0.50	0.63 ± 0.03	4.25 ± 0.89
SPT-CLJ0257-5732	44.3516	-57.5423	95 ± 19	5.28	4.53	3.51	5.40	0.25	0.4340	3.14 ± 0.86
SPT-CLJ0257-5842	44.3924	-58.7116	105 ± 21	5.35	5.19	4.71	5.38	1.00	0.42 ± 0.02	3.14 ± 0.86
SPT-CLJ0257-6050	44.3354	-60.8450	96 ± 23	4.46	4.68	4.32	4.76	1.25	0.48 ± 0.03	2.64 ± 0.86
SPT-CLJ0258-5756	44.5562	-57.9438	95 ± 22	4.06	4.50	4.18	4.50	1.50	>1.05 <sup>a</sup>	...
SPT-CLJ0300-6315	45.1430	-63.2643	73 ± 22	3.61	4.29	4.85	4.88	2.75	>1.50 <sup>a</sup>	...
SPT-CLJ0301-6456	45.4780	-64.9470	78 ± 20	4.79	4.07	2.99	4.94	0.25	0.65 ± 0.03	2.61 ± 0.82
SPT-CLJ0307-6226	46.8335	-62.4336	156 ± 20	8.15	8.09	6.94	8.32	0.75	0.61 ± 0.03	4.68 ± 0.96
SPT-CLJ0311-6354	47.8283	-63.9083	136 ± 20	7.06	7.11	6.29	7.33	1.00	0.30 ± 0.02	4.46 ± 0.96
SPT-CLJ0313-5645	48.2604	-56.7554	90 ± 20	4.70	4.50	3.82	4.82	0.75	0.63 ± 0.03	2.54 ± 0.82
SPT-CLJ0316-6059	49.2179	-60.9849	92 ± 19	4.45	3.95	3.28	4.59	0.25	>1.50 <sup>a</sup>	...
SPT-CLJ0317-5935	49.3208	-59.5856	100 ± 19	5.80	5.00	4.00	5.91	0.25	0.4690	3.46 ± 0.89
SPT-CLJ0320-5800	50.0316	-58.0084	74 ± 21	3.93	4.47	4.42	4.54	2.25	>0.99 <sup>a</sup>	...
SPT-CLJ0324-6236	51.0530	-62.6018	163 ± 19	8.59	8.01	6.82	8.59	0.50	0.74 ± 0.03	4.68 ± 0.96
SPT-CLJ0328-5541	52.1663	-55.6975	151 ± 23	6.71	6.98	6.75	7.08	1.75	0.0844	4.50 ± 1.00
SPT-CLJ0333-5842	53.3195	-58.7019	81 ± 21	4.43	4.54	4.31	4.54	1.50	0.49 ± 0.04	2.43 ± 0.86
SPT-CLJ0337-6207	54.4720	-62.1176	89 ± 21	4.32	4.84	4.75	4.88	1.75	>1.28 <sup>a</sup>	...
SPT-CLJ0337-6300	54.4685	-63.0098	84 ± 20	5.27	4.80	4.34	5.29	0.25	0.46 ± 0.03	3.07 ± 0.86
SPT-CLJ0341-5731	55.3979	-57.5233	95 ± 19	5.33	4.57	3.45	5.35	0.25	0.64 ± 0.02	2.96 ± 0.82
SPT-CLJ0341-6143	55.3485	-61.7192	119 ± 25	4.22	5.01	5.34	5.60	3.00	0.63 ± 0.03	3.11 ± 0.82
SPT-CLJ0343-5518	55.7634	-55.3049	104 ± 19	5.82	4.88	3.47	5.98	0.25	0.49 ± 0.02	3.50 ± 0.86
SPT-CLJ0344-5452	56.0926	-54.8725	96 ± 19	5.30	4.25	3.08	5.41	0.25	1.01 ± 0.07	2.68 ± 0.75
SPT-CLJ0344-5518	56.2101	-55.3037	94 ± 24	4.95	4.99	4.85	5.02	1.75	0.36 ± 0.02	2.89 ± 0.89
SPT-CLJ0345-6419	56.2518	-64.3326	93 ± 19	5.50	4.95	4.04	5.57	0.25	0.93 ± 0.07	2.86 ± 0.79
SPT-CLJ0346-5839	56.5745	-58.6535	87 ± 20	4.95	4.44	3.50	4.96	0.25	0.74 ± 0.07	2.57 ± 0.79
SPT-CLJ0351-5636	57.9312	-56.6099	88 ± 21	4.44	4.52	4.24	4.65	0.75	0.38 ± 0.03	2.61 ± 0.89
SPT-CLJ0351-5944	57.8654	-59.7457	76 ± 21	4.46	4.73	4.38	4.61	1.75	>0.99 <sup>a</sup>	...
SPT-CLJ0352-5647	58.2366	-56.7992	127 ± 20	7.02	6.97	6.25	7.11	0.75	0.66 ± 0.03	4.00 ± 0.86
SPT-CLJ0354-5904	58.5611	-59.0740	133 ± 22	6.20	6.30	5.72	6.49	1.25	0.41 ± 0.03	3.89 ± 0.89
SPT-CLJ0354-6032	58.6744	-60.5386	68 ± 19	4.38	3.13	2.25	4.57	0.25	1.06 ± 0.07	2.04 ± 0.75
SPT-CLJ0402-6129	60.7066	-61.4988	96 ± 22	4.81	4.76	4.33	4.83	1.00	0.53 ± 0.04	2.64 ± 0.86
SPT-CLJ0403-5534	60.9479	-55.5829	92 ± 21	4.44	4.78	4.67	4.88	1.75	>1.50 <sup>a</sup>	...
SPT-CLJ0403-5719	60.9670	-57.3241	98 ± 19	5.71	5.07	4.18	5.75	0.25	0.43 ± 0.02	3.39 ± 0.89
SPT-CLJ0404-6510	61.0556	-65.1817	113 ± 29	4.28	4.58	4.59	4.75	2.25	0.15 ± 0.02	2.86 ± 0.93
SPT-CLJ0406-5455	61.6922	-54.9205	100 ± 21	5.77	4.85	4.04	5.82	0.25	0.73 ± 0.03	3.18 ± 0.82
SPT-CLJ0410-5454	62.6154	-54.9016	87 ± 21	4.93	4.17	3.24	5.06	0.25	>0.98 <sup>a</sup>	...
SPT-CLJ0410-6343	62.5158	-63.7285	101 ± 19	5.79	5.27	4.31	5.79	0.50	0.49 ± 0.02	3.36 ± 0.86
SPT-CLJ0411-5751	62.8432	-57.8636	95 ± 21	4.71	5.04	4.69	5.16	1.25	0.75 ± 0.02	2.71 ± 0.79
SPT-CLJ0411-6340	62.8597	-63.6810	106 ± 19	6.28	5.63	4.80	6.41	0.25	0.14 ± 0.02	4.04 ± 0.96
SPT-CLJ0412-5743	63.0245	-57.7203	98 ± 21	5.11	5.24	4.87	5.29	1.25	0.38 ± 0.03	3.11 ± 0.89
SPT-CLJ0416-6359	64.1618	-63.9964	107 ± 20	6.03	5.63	4.85	6.06	0.75	0.30 ± 0.02	3.68 ± 0.89

**Table 6**  
(Continued)

ID and Coordinates			$Y_{SZ} \times 10^6$	Significances			Best		Redshift	$M_{500}$
SPT ID	R.A.	Decl.	(arcmin <sup>2</sup> )	$\theta_c = 0'.5$	1'.5	2'.5	$\xi$	$\theta_c$		( $10^{14} h_{70}^{-1} M_{\odot}$ )
SPT-CLJ0423-5506	65.8153	-55.1036	68 ± 22	4.06	4.42	3.91	4.51	1.25	0.21 ± 0.04	2.61 ± 0.89
SPT-CLJ0423-6143	65.9366	-61.7183	76 ± 20	4.46	4.03	3.12	4.65	0.25	0.71 ± 0.04	2.36 ± 0.79
SPT-CLJ0426-5455	66.5205	-54.9201	163 ± 19	8.86	7.94	6.70	8.86	0.50	0.63 ± 0.03	4.93 ± 1.00
SPT-CLJ0428-6049	67.0291	-60.8302	89 ± 21	4.74	4.89	4.20	5.06	1.25	>1.11 <sup>a</sup>	...
SPT-CLJ0430-6251	67.7086	-62.8536	86 ± 19	5.16	4.56	3.48	5.20	0.25	0.38 ± 0.04	3.04 ± 0.89
SPT-CLJ0431-6126	67.8393	-61.4438	321 ± 54	4.24	5.48	6.36	6.40	3.00	0.0577	4.11 ± 0.96
SPT-CLJ0433-5630	68.2522	-56.5038	102 ± 21	5.02	5.34	5.27	5.35	1.75	0.6920	2.89 ± 0.82
SPT-CLJ0441-5859	70.4411	-58.9931	88 ± 22	3.89	4.36	4.52	4.54	2.25	>1.06 <sup>a</sup>	...
SPT-CLJ0444-5603	71.1130	-56.0566	88 ± 19	5.19	4.21	3.12	5.30	0.25	0.98 ± 0.07	2.61 ± 0.75
SPT-CLJ0446-5849	71.5160	-58.8226	136 ± 19	7.34	6.29	4.95	7.44	0.25	1.16 ± 0.07	3.68 ± 0.82
SPT-CLJ0452-5945	73.1282	-59.7622	85 ± 23	3.78	4.37	4.50	4.50	2.50	>0.66 <sup>a</sup>	...
SPT-CLJ0456-5623	74.1745	-56.3869	79 ± 19	4.76	4.32	3.41	4.76	0.50	0.66 ± 0.03	2.46 ± 0.82
SPT-CLJ0456-6141	74.1496	-61.6840	80 ± 19	4.79	4.05	3.42	4.84	0.25	0.41 ± 0.03	2.71 ± 0.86
SPT-CLJ0458-5741	74.6021	-57.6952	85 ± 23	3.94	4.56	4.91	4.91	2.50	>1.03 <sup>a</sup>	...
SPT-CLJ0502-6113	75.5400	-61.2315	79 ± 19	5.02	4.41	3.54	5.09	0.25	0.66 ± 0.03	2.75 ± 0.82
SPT-CLJ0509-5342*	77.3360	-53.7045	157 ± 25	6.61	6.04	5.09	6.61	0.50	0.4607	5.36 ± 0.71
SPT-CLJ0511-5154	77.9202	-51.9044	119 ± 24	5.63	4.73	3.86	5.63	0.50	0.6450	3.61 ± 0.96
SPT-CLJ0514-5118	78.6859	-51.3100	111 ± 29	4.61	4.82	4.52	4.82	1.50	>1.16 <sup>a</sup>	...
SPT-CLJ0516-5430	79.1480	-54.5062	241 ± 26	9.11	9.37	8.57	9.42	0.75	0.2950	6.46 ± 1.32
SPT-CLJ0521-5104	80.2983	-51.0812	134 ± 28	5.34	5.28	4.96	5.45	1.00	0.6755	3.46 ± 0.96
SPT-CLJ0522-5026	80.5190	-50.4409	121 ± 32	4.50	4.82	4.72	4.87	1.75	0.51 ± 0.03	3.07 ± 1.00
SPT-CLJ0527-5928	81.8111	-59.4833	80 ± 25	4.52	3.66	3.14	4.71	0.25	>0.93 <sup>a</sup>	...
SPT-CLJ0528-5300*	82.0173	-53.0001	110 ± 23	5.42	4.38	3.52	5.45	0.25	0.7678	3.18 ± 0.61
SPT-CLJ0529-5238	82.2923	-52.6417	86 ± 24	4.31	3.50	2.68	4.52	0.25	>1.12 <sup>a</sup>	...
SPT-CLJ0532-5647	83.1586	-56.7893	99 ± 32	3.19	4.09	4.41	4.51	2.75	>0.93 <sup>a</sup>	...
SPT-CLJ0533-5005*	83.3984	-50.0918	116 ± 24	5.51	5.08	4.32	5.59	0.25	0.8810	2.68 ± 0.61
SPT-CLJ0534-5937	83.6018	-59.6289	82 ± 25	4.25	3.53	2.78	4.57	0.25	0.5761	2.71 ± 1.00
SPT-CLJ0537-5549	84.2578	-55.8268	100 ± 30	3.91	4.51	4.55	4.55	2.00	>1.11 <sup>a</sup>	...
SPT-CLJ0538-5657	84.5865	-56.9530	102 ± 30	3.79	4.37	4.61	4.63	2.75	>1.50 <sup>a</sup>	...
SPT-CLJ0539-5744	84.9998	-57.7432	109 ± 25	5.01	4.61	3.86	5.12	0.25	0.76 ± 0.03	3.07 ± 0.93
SPT-CLJ0546-5345*	86.6541	-53.7615	173 ± 24	7.69	6.99	6.20	7.69	0.50	1.0663	5.25 ± 0.75
SPT-CLJ0551-5709*	87.9016	-57.1565	150 ± 28	6.00	6.06	5.48	6.13	1.00	0.4230	3.75 ± 0.54
SPT-CLJ0556-5403	89.2016	-54.0630	100 ± 25	4.72	4.41	3.79	4.83	0.25	0.93 ± 0.04	2.64 ± 0.93
SPT-CLJ0559-5249*	89.9245	-52.8265	228 ± 26	8.81	9.15	8.51	9.28	1.00	0.6090	6.79 ± 0.86
SPT-CLJ2002-5335	300.5113	-53.5913	75 ± 23	4.44	4.30	4.01	4.53	1.25	>1.02 <sup>a</sup>	...
SPT-CLJ2005-5635	301.3385	-56.5902	80 ± 19	4.68	4.38	3.88	4.68	0.50	>0.64 <sup>a</sup>	...
SPT-CLJ2006-5325	301.6620	-53.4287	86 ± 23	4.93	4.77	4.01	5.06	1.00	>1.50 <sup>a</sup>	...
SPT-CLJ2007-4906	301.9663	-49.1105	87 ± 23	4.46	3.84	3.14	4.50	0.25	1.25 ± 0.07	1.93 ± 0.86
SPT-CLJ2009-5756	302.4262	-57.9480	80 ± 19	4.68	4.20	3.42	4.68	0.50	0.63 ± 0.03	2.36 ± 0.79
SPT-CLJ2011-5228	302.7810	-52.4734	75 ± 23	4.46	4.21	3.70	4.55	0.75	0.96 ± 0.04	2.25 ± 0.89
SPT-CLJ2011-5725	302.8526	-57.4214	91 ± 19	5.35	5.25	4.83	5.43	0.75	0.2786	3.18 ± 0.89
SPT-CLJ2012-5342	303.0822	-53.7137	73 ± 23	4.65	4.38	3.84	4.65	0.50	>0.68 <sup>a</sup>	...
SPT-CLJ2012-5649	303.1132	-56.8308	116 ± 25	4.70	5.83	5.99	5.99	2.50	0.0552	3.71 ± 0.93
SPT-CLJ2013-5432	303.4968	-54.5445	78 ± 23	4.23	3.05	1.92	4.75	0.25	>1.02 <sup>a</sup>	...
SPT-CLJ2015-5504	303.9884	-55.0715	79 ± 23	4.64	4.28	3.68	4.64	0.50	>0.61 <sup>a</sup>	...
SPT-CLJ2016-4954	304.0181	-49.9122	100 ± 23	5.01	4.62	3.77	5.01	0.50	0.26 ± 0.02	3.25 ± 0.96
SPT-CLJ2017-6258	304.4827	-62.9763	117 ± 22	5.89	6.45	5.92	6.45	1.50	0.57 ± 0.03	3.61 ± 0.82
SPT-CLJ2018-4528	304.6076	-45.4807	85 ± 23	4.59	4.26	3.41	4.64	0.25	0.40 ± 0.03	2.82 ± 0.96
SPT-CLJ2019-5642	304.7703	-56.7079	94 ± 19	5.17	5.05	4.41	5.25	0.75	0.15 ± 0.03	3.11 ± 0.89
SPT-CLJ2020-4646	305.1936	-46.7702	97 ± 24	5.07	5.08	4.38	5.09	1.25	0.17 ± 0.02	3.43 ± 1.00
SPT-CLJ2020-6314	305.0301	-63.2413	82 ± 19	5.31	4.69	3.84	5.37	0.25	0.58 ± 0.02	2.89 ± 0.82
SPT-CLJ2021-5256	305.4690	-52.9439	190 ± 54	3.44	4.58	5.27	5.31	3.00	0.11 ± 0.02	3.64 ± 1.00
SPT-CLJ2022-6323	305.5235	-63.3973	106 ± 19	6.58	5.91	5.04	6.58	0.50	0.3830	3.82 ± 0.89
SPT-CLJ2023-5535	305.8377	-55.5903	282 ± 24	11.75	13.36	13.04	13.41	1.75	0.2320	7.14 ± 1.43
SPT-CLJ2025-5117	306.4837	-51.2904	183 ± 22	9.37	8.81	7.36	9.48	0.75	0.20 ± 0.02	6.29 ± 1.29
SPT-CLJ2026-4513	306.6140	-45.2256	107 ± 22	5.53	5.09	4.26	5.53	0.50	0.71 ± 0.03	3.32 ± 0.89
SPT-CLJ2030-5638	307.7067	-56.6352	100 ± 20	5.28	5.33	4.89	5.47	1.00	0.39 ± 0.03	3.14 ± 0.86
SPT-CLJ2032-5627	308.0800	-56.4557	167 ± 22	7.64	8.03	7.92	8.14	1.75	0.2840	4.79 ± 1.00
SPT-CLJ2034-5936	308.5408	-59.6007	144 ± 18	8.54	7.62	6.23	8.57	0.25	0.92 ± 0.07	4.32 ± 0.89
SPT-CLJ2035-5251	308.8026	-52.8527	205 ± 23	9.60	9.95	8.97	10.00	0.75	0.47 ± 0.02	6.18 ± 1.25
SPT-CLJ2035-5614	308.9022	-56.2407	76 ± 19	4.43	4.27	3.70	4.55	0.75	>1.02 <sup>a</sup>	...
SPT-CLJ2039-5723	309.8246	-57.3871	76 ± 19	4.69	4.34	4.13	4.69	0.50	>1.25 <sup>a</sup>	...
SPT-CLJ2040-4451	310.2468	-44.8599	122 ± 22	6.08	4.60	3.62	6.28	0.25	1.35 ± 0.07	3.21 ± 0.79
SPT-CLJ2040-5230	310.1255	-52.5052	76 ± 22	4.50	3.41	2.57	4.70	0.25	>1.01 <sup>a</sup>	...

**Table 6**  
(Continued)

ID and Coordinates			$Y_{SZ} \times 10^6$	Significances			Best		Redshift	$M_{500}$
SPT ID	R.A.	Decl.	(arcmin <sup>2</sup> )	$\theta_c = 0'.5$	$1'.5$	$2'.5$	$\xi$	$\theta_c$		( $10^{14} h_{70}^{-1} M_{\odot}$ )
SPT-CLJ2040-5342	310.2195	-53.7122	107 ± 22	5.88	5.36	4.61	5.88	0.50	0.57 ± 0.04	3.68 ± 0.89
SPT-CLJ2040-5725	310.0631	-57.4287	107 ± 19	6.38	5.91	5.03	6.38	0.50	0.9300	3.25 ± 0.75
SPT-CLJ2043-5035	310.8285	-50.5929	151 ± 22	7.81	7.47	6.73	7.81	0.50	0.7234	4.71 ± 1.00
SPT-CLJ2043-5614	310.7906	-56.2351	74 ± 19	4.66	4.00	3.17	4.72	0.25	0.69 ± 0.03	2.36 ± 0.79
SPT-CLJ2045-6026	311.3649	-60.4469	67 ± 19	4.59	3.46	2.51	4.77	0.25	>0.47 <sup>a</sup>	...
SPT-CLJ2046-4542	311.5620	-45.7111	92 ± 23	4.43	4.36	3.73	4.54	1.00	>1.02 <sup>a</sup>	...
SPT-CLJ2048-4524	312.2268	-45.4150	89 ± 24	4.25	4.44	3.96	4.56	1.00	>0.98 <sup>a</sup>	...
SPT-CLJ2051-6256	312.8027	-62.9348	83 ± 20	4.97	5.04	4.39	5.17	1.25	0.47 ± 0.02	2.86 ± 0.86
SPT-CLJ2055-5456	313.9941	-54.9366	113 ± 18	6.61	6.32	5.71	6.61	0.50	0.11 ± 0.02	4.64 ± 1.07
SPT-CLJ2056-5106	314.0723	-51.1163	89 ± 25	4.37	4.60	4.63	4.70	2.00	>1.02 <sup>a</sup>	...
SPT-CLJ2056-5459	314.2199	-54.9892	102 ± 19	5.87	5.07	4.23	6.05	0.25	0.7180	3.68 ± 0.89
SPT-CLJ2057-5251	314.4105	-52.8567	69 ± 23	4.50	4.03	3.38	4.52	0.25	>1.50 <sup>a</sup>	...
SPT-CLJ2058-5608	314.5893	-56.1454	78 ± 18	4.84	4.03	2.88	5.02	0.25	0.6060	2.64 ± 0.79
SPT-CLJ2059-5018	314.9324	-50.3049	91 ± 22	4.73	4.21	3.30	4.79	0.25	0.39 ± 0.02	2.96 ± 0.96
SPT-CLJ2100-4548	315.0936	-45.8057	90 ± 23	4.84	4.53	4.12	4.84	0.50	0.7121	2.71 ± 0.93
SPT-CLJ2100-5708	315.1503	-57.1347	83 ± 19	5.03	4.47	3.21	5.11	0.25	0.59 ± 0.03	2.71 ± 0.79
SPT-CLJ2101-5542	315.3106	-55.7027	115 ± 29	4.67	4.99	4.82	5.04	1.75	0.22 ± 0.02	2.93 ± 0.86
SPT-CLJ2101-6123	315.4594	-61.3972	84 ± 19	5.28	4.83	3.95	5.28	0.50	0.60 ± 0.03	2.82 ± 0.82
SPT-CLJ2103-5411	315.7687	-54.1951	78 ± 22	4.72	4.32	3.48	4.88	0.25	0.46 ± 0.02	2.96 ± 0.96
SPT-CLJ2104-5224	316.2283	-52.4044	77 ± 23	4.97	3.54	2.19	5.32	0.25	0.7991	3.04 ± 0.89
SPT-CLJ2106-5820	316.5144	-58.3459	66 ± 19	4.43	2.94	1.56	4.81	0.25	>1.00 <sup>a</sup>	...
SPT-CLJ2106-5844	316.5210	-58.7448	363 ± 18	21.78	18.67	14.36	22.08	0.25	1.1320	8.36 ± 1.71
SPT-CLJ2106-6019	316.6642	-60.3299	73 ± 19	4.82	3.49	2.21	4.98	0.25	0.97 ± 0.03	2.32 ± 0.75
SPT-CLJ2106-6303	316.6596	-63.0510	84 ± 20	4.56	4.82	4.24	4.90	1.25	>1.04 <sup>a</sup>	...
SPT-CLJ2109-4626	317.4516	-46.4370	104 ± 21	5.32	4.33	3.24	5.51	0.25	0.98 ± 0.09	3.00 ± 0.86
SPT-CLJ2109-5040	317.3820	-50.6773	103 ± 27	4.56	5.14	5.06	5.17	2.00	0.47 ± 0.03	3.21 ± 0.93
SPT-CLJ2110-5244	317.5502	-52.7486	114 ± 22	6.22	5.82	4.79	6.22	0.50	0.61 ± 0.02	3.86 ± 0.93
SPT-CLJ2111-5338	317.9216	-53.6496	111 ± 25	5.53	5.51	4.80	5.65	1.00	0.43 ± 0.03	3.64 ± 0.93
SPT-CLJ2115-4659	318.7995	-46.9862	140 ± 34	4.98	5.40	5.48	5.60	2.25	0.34 ± 0.02	3.68 ± 0.96
SPT-CLJ2118-5055	319.7291	-50.9329	116 ± 22	5.52	4.84	3.66	5.62	0.25	0.6254	3.43 ± 0.93
SPT-CLJ2119-6230	319.8846	-62.5096	61 ± 19	4.37	3.35	2.83	4.55	0.25	0.72 ± 0.03	2.21 ± 0.79
SPT-CLJ2120-4728	320.1594	-47.4776	109 ± 21	5.87	4.82	3.61	5.98	0.25	0.99 ± 0.07	3.36 ± 0.86
SPT-CLJ2121-5546	320.2715	-55.7780	85 ± 19	4.61	4.44	3.55	4.79	0.75	>0.75 <sup>a</sup>	...
SPT-CLJ2121-6335	320.4269	-63.5843	133 ± 32	3.87	5.01	5.43	5.43	2.75	0.23 ± 0.02	3.21 ± 0.86
SPT-CLJ2124-6124	321.1488	-61.4141	147 ± 21	8.08	8.18	7.70	8.21	1.00	0.4350	4.68 ± 0.96
SPT-CLJ2125-6113	321.2902	-61.2292	76 ± 19	4.74	4.55	4.27	4.74	0.50	>1.50 <sup>a</sup>	...
SPT-CLJ2127-6443	321.9939	-64.7288	75 ± 22	3.81	4.44	4.53	4.54	1.75	>0.97 <sup>a</sup>	...
SPT-CLJ2130-4737	322.6622	-47.6257	81 ± 23	4.51	3.37	2.18	4.83	0.25	>1.50 <sup>a</sup>	...
SPT-CLJ2130-6458	322.7285	-64.9764	130 ± 20	7.31	7.31	6.43	7.57	1.00	0.3160	4.46 ± 0.96
SPT-CLJ2131-5003	322.9717	-50.0647	88 ± 23	4.83	4.50	3.98	4.83	0.50	0.45 ± 0.02	2.93 ± 0.93
SPT-CLJ2133-5411	323.2978	-54.1845	71 ± 22	4.17	3.00	1.75	4.58	0.25	>1.50 <sup>a</sup>	...
SPT-CLJ2135-5452	323.9060	-54.8773	90 ± 20	4.39	4.57	4.00	4.61	1.00	>1.00 <sup>a</sup>	...
SPT-CLJ2135-5726	323.9158	-57.4415	176 ± 18	10.43	9.81	8.64	10.43	0.50	0.4270	5.68 ± 1.11
SPT-CLJ2136-4704	324.1175	-47.0803	114 ± 22	6.10	5.46	4.68	6.17	0.25	0.4250	4.04 ± 0.96
SPT-CLJ2136-5519	324.2392	-55.3215	73 ± 19	4.65	3.91	3.37	4.65	0.50	>1.50 <sup>a</sup>	...
SPT-CLJ2136-5535	324.0898	-55.5853	74 ± 19	4.52	4.40	3.79	4.58	0.75	>1.19 <sup>a</sup>	...
SPT-CLJ2136-5723	324.1209	-57.3923	75 ± 20	4.22	4.55	4.10	4.55	1.50	>1.04 <sup>a</sup>	...
SPT-CLJ2136-6307	324.2334	-63.1233	100 ± 19	6.11	5.80	4.91	6.25	0.75	0.9260	3.18 ± 0.75
SPT-CLJ2137-6437	324.4178	-64.6235	71 ± 19	4.40	4.10	3.27	4.60	0.75	0.91 ± 0.07	2.11 ± 0.75
SPT-CLJ2138-6007	324.5060	-60.1324	225 ± 19	12.39	12.41	11.14	12.64	0.75	0.3190	6.75 ± 1.32
SPT-CLJ2139-5420	324.9670	-54.3396	77 ± 24	4.69	4.69	3.92	4.81	0.75	0.24 ± 0.02	3.07 ± 1.00
SPT-CLJ2140-5331	325.0304	-53.5199	90 ± 23	4.54	4.13	3.48	4.55	0.25	0.51 ± 0.02	2.61 ± 0.96
SPT-CLJ2140-5727	325.1380	-57.4564	76 ± 19	4.90	4.01	3.14	5.08	0.25	0.40 ± 0.03	2.86 ± 0.86
SPT-CLJ2142-4846	325.5693	-48.7743	70 ± 24	4.02	4.53	4.36	4.53	1.50	>0.80 <sup>a</sup>	...
SPT-CLJ2145-5644	326.4694	-56.7477	213 ± 18	12.30	11.67	10.39	12.30	0.50	0.4800	6.39 ± 1.25
SPT-CLJ2146-4633	326.6473	-46.5505	202 ± 22	9.59	8.67	6.99	9.59	0.50	0.9330	5.36 ± 1.07
SPT-CLJ2146-4846	326.5346	-48.7774	115 ± 25	5.59	5.88	5.34	5.88	1.50	0.6230	3.64 ± 0.93
SPT-CLJ2146-5736	326.6963	-57.6138	98 ± 19	5.94	5.46	4.57	5.94	0.50	0.61 ± 0.02	3.25 ± 0.82
SPT-CLJ2148-4843	327.0971	-48.7287	77 ± 23	4.19	2.88	1.81	4.64	0.25	0.98 ± 0.07	2.29 ± 0.86
SPT-CLJ2148-6116	327.1798	-61.2791	124 ± 20	6.95	7.22	6.31	7.27	1.25	0.5710	4.04 ± 0.89
SPT-CLJ2149-5330	327.3770	-53.5014	95 ± 24	4.79	4.50	4.04	4.79	0.50	0.60 ± 0.03	2.79 ± 0.93
SPT-CLJ2150-6111	327.7177	-61.1954	73 ± 21	4.12	4.50	4.70	4.70	2.50	>1.11 <sup>a</sup>	...
SPT-CLJ2152-4629	328.1943	-46.4947	94 ± 21	5.45	4.56	3.26	5.60	0.25	>1.50 <sup>a</sup>	...
SPT-CLJ2152-5143	328.0034	-51.7245	67 ± 24	4.45	4.33	3.79	4.53	0.75	0.41 ± 0.03	2.68 ± 0.96
SPT-CLJ2152-5633	328.1458	-56.5641	100 ± 21	5.16	5.66	5.68	5.84	1.75	>1.50 <sup>a</sup>	...

**Table 6**  
(Continued)

ID and Coordinates			$Y_{SZ} \times 10^6$	Significances			Best		Redshift	$M_{500}$
SPT ID	R.A.	Decl.	(arcmin <sup>2</sup> )	$\theta_c = 0'.5$	1'.5	2'.5	$\xi$	$\theta_c$		( $10^{14} h_{70}^{-1} M_{\odot}$ )
SPT-CLJ2155-5103	328.8747	-51.0508	73 ± 25	4.11	4.41	4.40	4.52	1.75	>1.06 <sup>a</sup>	...
SPT-CLJ2155-5225	328.8941	-52.4169	95 ± 25	4.45	4.77	4.36	4.77	1.50	0.62 ± 0.03	2.71 ± 0.93
SPT-CLJ2155-6048	328.9851	-60.8072	88 ± 20	4.87	5.19	4.56	5.24	1.00	0.5390	2.82 ± 0.82
SPT-CLJ2158-4702	329.6901	-47.0348	78 ± 23	4.50	4.38	4.17	4.56	1.00	>0.90 <sup>a</sup>	...
SPT-CLJ2158-4851	329.5737	-48.8536	80 ± 23	4.28	3.38	2.20	4.61	0.25	>0.75 <sup>a</sup>	...
SPT-CLJ2158-5615	329.5975	-56.2588	88 ± 20	4.28	4.42	3.93	4.54	1.25	>1.07 <sup>a</sup>	...
SPT-CLJ2158-6319	329.6390	-63.3175	62 ± 19	4.33	3.43	2.64	4.54	0.25	>1.06 <sup>a</sup>	...
SPT-CLJ2159-6244	329.9922	-62.7420	108 ± 21	6.02	5.98	5.54	6.08	1.00	0.43 ± 0.02	3.50 ± 0.86
SPT-CLJ2200-5547	330.0304	-55.7954	79 ± 21	3.83	4.63	4.72	4.80	2.00	>0.98 <sup>a</sup>	...
SPT-CLJ2201-5956	330.4727	-59.9473	338 ± 25	11.61	13.57	13.99	13.99	2.50	0.0972	7.57 ± 1.50
SPT-CLJ2202-5936	330.5483	-59.6021	76 ± 19	4.81	4.21	3.36	4.89	0.25	0.42 ± 0.03	2.68 ± 0.82
SPT-CLJ2259-5432	344.9820	-54.5356	135 ± 38	4.56	4.71	4.65	4.78	2.00	0.46 ± 0.03	3.04 ± 1.04
SPT-CLJ2259-5617	344.9974	-56.2877	99 ± 24	5.04	4.27	3.55	5.29	0.25	0.15 ± 0.02	3.79 ± 1.07
SPT-CLJ2300-5331	345.1765	-53.5170	119 ± 27	5.24	5.02	4.65	5.29	0.25	0.2620	3.68 ± 1.04
SPT-CLJ2301-5046	345.4585	-50.7823	92 ± 24	4.58	3.83	2.82	4.58	0.50	>1.50 <sup>a</sup>	...
SPT-CLJ2301-5546	345.4688	-55.7758	106 ± 25	5.19	4.93	4.62	5.19	0.50	0.7480	3.11 ± 0.96
SPT-CLJ2302-5225	345.6464	-52.4329	104 ± 29	3.77	4.24	4.60	4.60	2.50	>1.04 <sup>a</sup>	...
SPT-CLJ2311-5011	347.8427	-50.1838	91 ± 29	3.40	3.85	4.42	4.64	3.00	>1.50 <sup>a</sup>	...
SPT-CLJ2312-5820	348.0002	-58.3419	89 ± 24	4.66	3.75	3.11	4.78	0.25	0.83 ± 0.05	2.68 ± 0.96
SPT-CLJ2329-5831	352.4760	-58.5238	107 ± 25	4.95	4.64	3.96	4.95	0.50	0.81 ± 0.03	2.86 ± 0.93
SPT-CLJ2331-5051*	352.9584	-50.8641	166 ± 23	7.86	6.60	5.14	8.04	0.25	0.5760	5.14 ± 0.71
SPT-CLJ2332-5358*	353.1040	-53.9733	193 ± 31	7.25	7.30	6.84	7.30	1.50	0.4020	6.50 ± 0.79
SPT-CLJ2334-5953	353.6989	-59.8892	94 ± 30	2.94	3.98	4.53	4.53	2.50	>1.50 <sup>a</sup>	...
SPT-CLJ2337-5942*	354.3544	-59.7052	312 ± 24	14.72	12.63	10.11	14.94	0.25	0.7750	8.14 ± 1.14
SPT-CLJ2341-5119*	355.2994	-51.3328	227 ± 24	9.48	9.02	7.74	9.65	0.75	1.0030	5.61 ± 0.82
SPT-CLJ2342-5411*	355.6903	-54.1887	132 ± 23	6.18	5.24	3.96	6.18	0.50	1.0750	3.00 ± 0.50
SPT-CLJ2343-5521	355.7574	-55.3641	130 ± 28	4.87	5.58	5.74	5.74	2.50	>1.50 <sup>a</sup>	...
SPT-CLJ2343-5556	355.9290	-55.9371	106 ± 27	4.49	4.53	4.00	4.58	1.00	>1.22 <sup>a</sup>	...
SPT-CLJ2351-5452	357.8877	-54.8753	151 ± 47	4.35	4.70	4.83	4.89	2.75	0.3838	3.18 ± 1.04
SPT-CLJ2355-5056*	358.9551	-50.9367	138 ± 24	5.73	5.34	4.31	5.89	0.75	0.3196	4.07 ± 0.57
SPT-CLJ2359-5009*	359.9208	-50.1600	152 ± 27	6.19	6.23	5.64	6.35	1.25	0.7750	3.54 ± 0.54

**Notes.** Galaxy cluster candidates selected above a significance of 4.5 in the first 720 deg<sup>2</sup> of the SPT survey. Galaxy clusters marked by an “\*” have X-ray data that are used in the cosmological analysis (see A11 and B11 for a description of the X-ray data). For each candidate, we report the detection significance of each candidate in the “Best” column, as well as the significances at a fixed set of three core radii (Section 3). We also report the position and (if confirmed) redshift (Section 4). Spectroscopic redshifts are quoted without uncertainties. The integrated  $Y_{SZ}$  is reported for a 1' aperture (Section 3.3). Finally, we report a mass estimate for each confirmed cluster marginalized over the  $\Lambda$ CDM chain (Section 7.1.2).

<sup>a</sup> Unconfirmed cluster candidate which is either above the quoted redshift limit or a false detection.

(This table is also available in a machine-readable form in the online journal.)

high-redshift clusters is small compared to the expected number of false detections.

## 7. COSMOLOGICAL IMPLICATIONS

We present cosmological constraints from the SPT cluster sample in this section. The main results are tabulated in Table 5. We first consider the baseline, six-parameter  $\Lambda$ CDM model, and highlight the improvement in parameter constraints for the current catalog compared to the smaller B11 catalog. The uncertainty in the cosmological analysis is dominated by the systematic cluster mass uncertainty; the mass calibration is based on the same X-ray data and  $Y_X - M$  scaling relation used in the analysis of B11. The  $Y_X - M$  scaling relation was observationally measured using X-ray measurements of the total mass derived assuming hydrostatic equilibrium, with the absolute calibration cross-checked by weak-lensing-based mass estimates. We also compare the observed and expected cluster abundances, and we estimate the masses of each galaxy cluster. We next examine cosmological constraints for two extensions beyond a  $\Lambda$ CDM model, testing the ability of the cluster sample to constrain the dark energy equation of state and

the sum of the neutrino masses. These two model extensions are degenerate in the current cluster data; we choose to look at independent constraints on each while fixing the other parameter to the  $\Lambda$ CDM baseline value. Finally, we discuss prospects for improving the mass calibration and thereby realizing the full potential of SZ-selected galaxy clusters as cosmological probes.

### 7.1. $\Lambda$ CDM Constraints

In a  $\Lambda$ CDM model, cluster samples primarily constrain  $\sigma_8$  and  $\Omega_m$  (see e.g., B11, Rozo et al. 2010). As was done by B11, we look at “cluster-only” constraints based on SPT<sub>CL</sub>+BBN+H<sub>0</sub> with the reionization optical depth fixed to  $\tau = 0.08$ . The external data and  $\tau$  prior are required since cluster abundances are insensitive to several  $\Lambda$ CDM parameters, including  $\tau$ . We see a substantial improvement in the SPT<sub>CL</sub>+BBN+H<sub>0</sub> constraints with the expanded cluster catalog from this work; the allowed likelihood volume is reduced by approximately a factor of two (compare the filled red/orange contours and black contours in Figure 5).

Adding the new SPT cluster sample to the WMAP7 and SPT CMB power spectrum data improves the constraints on

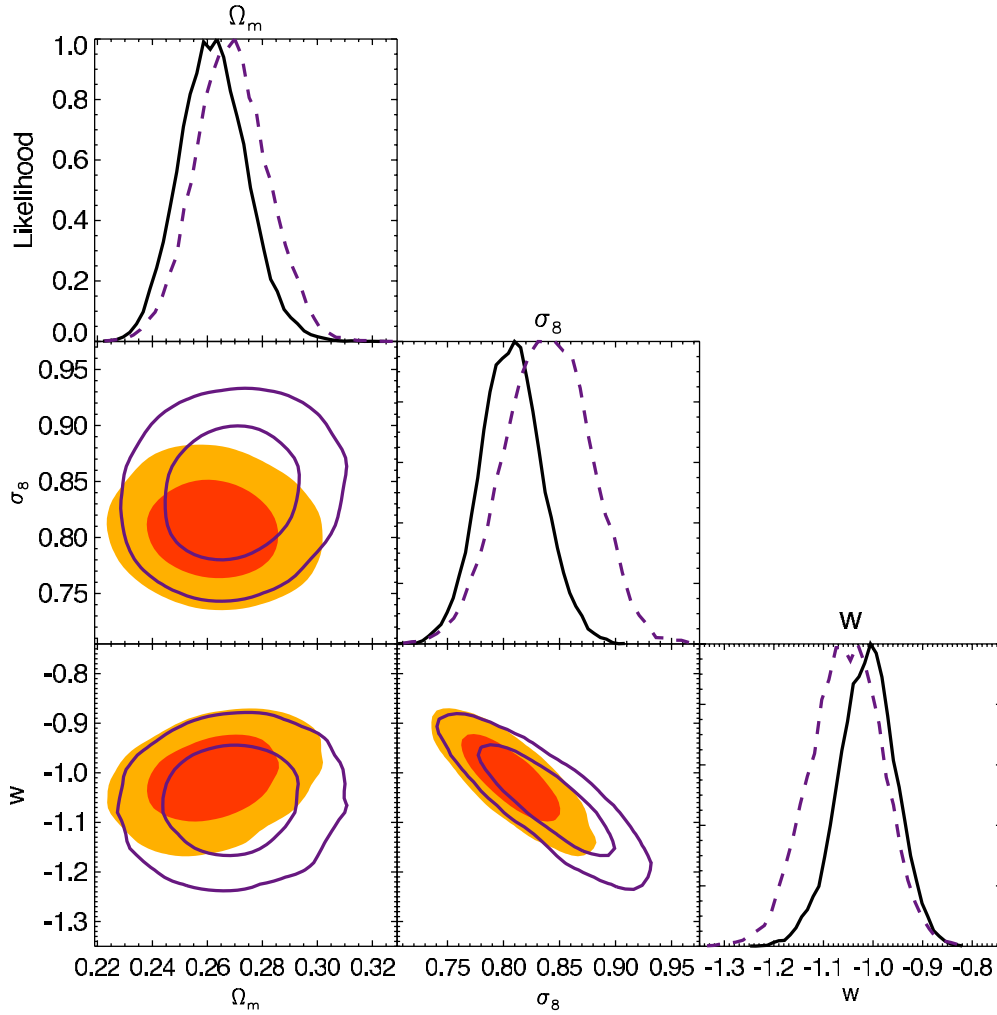


**Figure 6.** Assuming a  $w$ CDM cosmology, the constraints on  $\Omega_m$ ,  $\sigma_8$ , and  $w$ . The plots along the diagonal are the one-dimensional marginalized likelihood. The off-diagonal plots are the two-dimensional marginalized constraints showing the 68% and 95% confidence regions. We show the constraints for the CMB + BAO +  $H_0$  + SNe (purple line contours and dashed lines) and CMB + BAO +  $H_0$  + SNe + SPT<sub>CL</sub> (filled contours and black, solid lines) data sets. Including the SPT<sub>CL</sub> data improves the constraints on  $\Omega_m$ ,  $\sigma_8$ , and  $w$  by factors of 1.1, 1.4, and 1.3 respectively.

(A color version of this figure is available in the online journal.)

$\Omega_m$ ,  $\Omega_c h^2$ ,  $\sigma_8$ , and  $h$  by roughly a factor of 1.5 over the CMB alone. The constraints are listed in the first two columns of Table 5. The cluster data modestly tightens constraints on the amplitude of the primordial power spectrum as well. The uncertainty on the amplitude is reduced by 24% from  $\ln(10^{10} A_s) = 3.196 \pm 0.042$  to  $3.176 \pm 0.034$ .

However, these constraints are only marginally better than those presented by B11. As shown in Figure 5, the SPT<sub>CL</sub> constraints in the  $\Omega_m - \sigma_8$  plane are most improved along a direction well constrained by the CMB data. For constraints in the perpendicular direction, the SPT<sub>CL</sub> data are limited by the current mass calibration uncertainty, determined from the  $Y_X - M$  scaling relation which is unchanged from B11. The mass calibration uncertainty would need to be reduced by a factor of  $\sim 2.5$  to be comparable to the statistical uncertainty. A better mass calibration will be essential to realize the full potential of cosmological constraints from galaxy clusters.

#### 7.1.1. Comparison to Expected Number Counts

We can compare the observed number of galaxy clusters with the number expected for a given cosmological model. We compare the high-purity sample of 100 cluster candidates at

$z > 0.3$  and  $\xi > 5$  to the expected number counts for two cases with a  $\Lambda$ CDM cosmology. The first case uses only non-cluster data (CMB+BAO+SN+ $H_0$ ) with the scaling relations allowed to vary across the conservatively wide simulation-based prior. The likelihood peaks near 130 candidates, but is highly non-Gaussian. The 68% confidence interval around the median is [121, 805] candidates and the 95% confidence interval is [37, 2004] candidates. In the second case, we add the cluster catalog data while allowing the scaling relations to vary. As would be expected, this MCMC leads to a tighter predicted range of candidate counts with roughly Poisson scatter around the observed number counts. The  $1\sigma$  range is [92, 111] candidates with the median at 101 objects. The difference between the two cases is primarily due to the range of scaling relation parameters explored. We do not see significant tension with the observed cluster counts in either case.

#### 7.1.2. Mass Estimates

We present mass estimates based on the posterior probability distributions for all optically confirmed clusters in Table 6. In all cases, we quote  $M_{500}$ , as defined in Section 5. For the 15 clusters with X-ray data from A11, these are joint X-ray and SZ mass



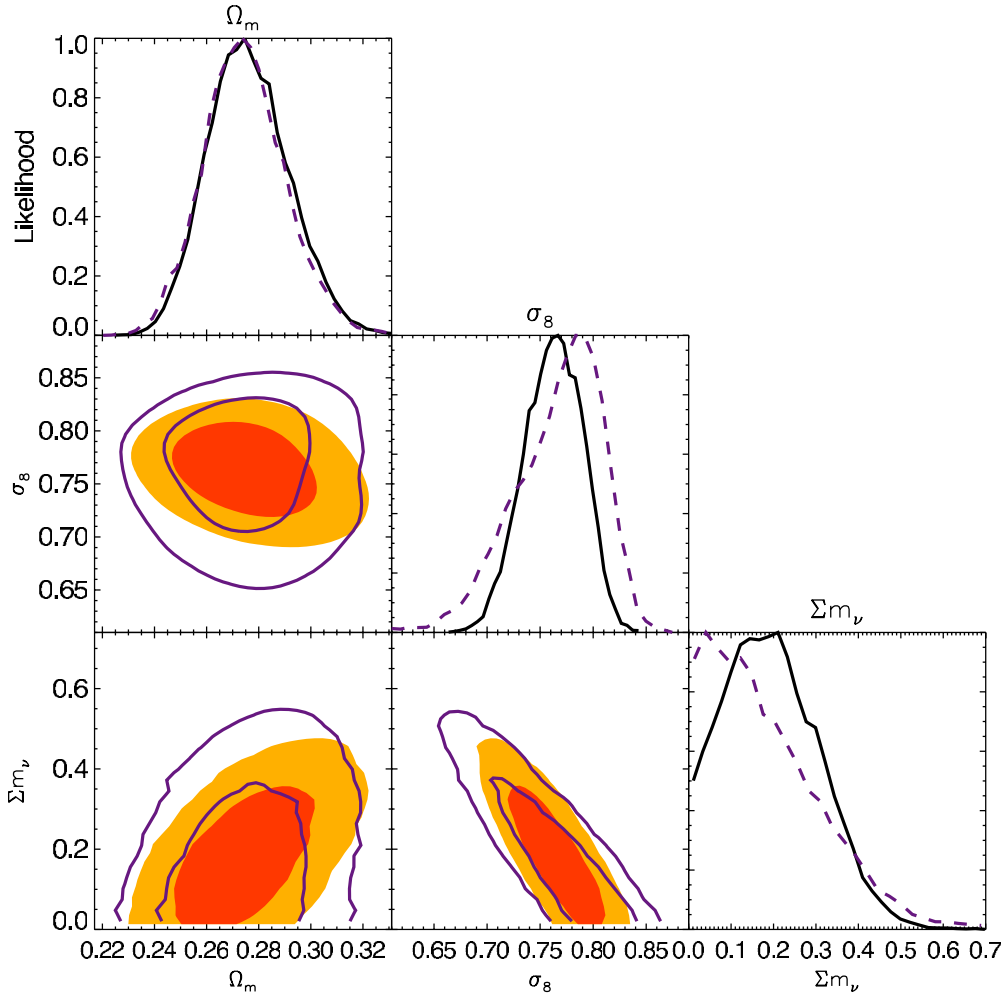


**Figure 7.** Assuming a  $\Lambda$ CDM + massive neutrino cosmology, the constraints on  $\Omega_m$ ,  $\sigma_8$ , and  $\Sigma m_\nu$ . The plots along the diagonal are the one-dimensional marginalized likelihood. The off-diagonal plots are the two-dimensional marginalized constraints showing the 68% and 95% confidence regions. We show the constraints for the CMB+BAO+ $H_0$  (purple line contours and dashed lines) and CMB+BAO+ $H_0$ +SPT<sub>CL</sub> (filled contours and black solid lines) data sets. The SPT<sub>CL</sub> data lead to a small preference for positive neutrino masses with  $\Sigma m_\nu = 0.17 \pm 0.13$  eV; the 95% CL upper limit on the neutrino masses is reduced from  $\Sigma m_\nu < 0.44$  eV to  $\Sigma m_\nu < 0.38$  eV.

(A color version of this figure is available in the online journal.)

estimates. Only the SZ data are used for the other clusters. We calculate a probability density function on a mass grid at each point in the CMB+BAO+SN+ $H_0$ +SPT<sub>CL</sub> parameter chain for a  $\Lambda$ CDM cosmology. The allowed  $\Lambda$ CDM parameter ranges for this data set are essentially unchanged from the CMB+SPT<sub>CL</sub> data set. These probability density functions are combined to obtain a mass estimate that has been fully marginalized over all cosmological and scaling relation parameters.

### 7.2. Dark Energy Equation of State

We next examine cosmological constraints in a wCDM cosmology. This model introduces the dark energy equation of state,  $w$ , as a free parameter (in the  $\Lambda$ CDM model,  $w$  is fixed to  $-1$ ). The equation of state remains constant with time. The cluster abundance and the shape of the mass function depend on  $w$  through its effect on the expansion history of the universe and the growth of structure.

The best external constraints on  $w$  come from a combination of the CMB, BAO,  $H_0$ , and SNe data. Adding the SPT cluster sample to this data set reduces the uncertainty on the dark energy equation of state by a factor of 1.3 to give  $-1.010 \pm 0.058$ . This

value is completely consistent with a cosmological constant and within  $1\sigma$  of the no-cluster constraint of  $w = -1.054 \pm 0.073$ . These results are shown in Figure 6 and tabulated in Table 5.

The cluster data also aid in the measurement of the dark matter density and  $\sigma_8$ . The addition of clusters moves the preferred cold dark matter density down by nearly  $1\sigma$  from  $\Omega_c h^2 = 0.1140 \pm 0.0041$  to  $\Omega_c h^2 = 0.1104 \pm 0.0029$ . As would be expected, the amplitude of the matter power spectrum also drops from  $\sigma_8 = 0.840 \pm 0.038$  to  $0.807 \pm 0.027$ . The uncertainties on both parameters are reduced by a factor of 1.4 with the addition of the SPT cluster data.

We can compare the wCDM results to those reported by B11 based on fewer clusters but the same X-ray data and mass calibration uncertainty. B11 report  $\sigma_8 = 0.793 \pm 0.028$  and  $w = -0.973 \pm 0.063$  for the CMB + BAO + SNe + SPT<sub>CL</sub> (B11) data. In this analysis, the median  $\sigma_8$  and  $w$  values shift by  $\sim 0.5\sigma$  relative those presented by B11, and the uncertainties tighten slightly. These changes are primarily due to including the local measurement of  $H_0$  in the constraints, rather than the additional clusters. We also ran chains without  $H_0$  to parallel the B11 treatment and both differences effectively disappear.

### 7.3. Massive Neutrinos

The second extension to a  $\Lambda$ CDM model that we consider is a non-zero sum of neutrino masses,  $\sum m_\nu \geq 0$ . Non-zero neutrino masses are well motivated by the measured mass differences in neutrino oscillation experiments (e.g., Ahmad et al. 2002; Eguchi et al. 2003; Ashie et al. 2004). For CMB+ $H_0$ +BAO, neutrino masses are highly degenerate with  $\sigma_8$ , as shown in Figure 7. Cluster abundances are an independent measure of local structure ( $\sigma_8$ ), and thereby enable better constraints on the sum of the neutrino masses. In this work, we assume a thermal background of three degenerate mass neutrino species.

The main results with massive neutrinos are shown in Figure 7 and tabulated in Table 5. Adding the SPT cluster sample to the CMB+ $H_0$ +BAO data leads to a small preference for a positive neutrino mass sum. If we fit the 1D posterior on the total neutrino mass with a Gaussian (avoiding the bias to the median and 68% interval values due to the positivity prior), the preferred value is  $\sum m_\nu = 0.17 \pm 0.13$  eV. The uncertainties on the neutrino mass tighten with the addition of the cluster data, but the shift in the peak likelihood toward higher masses means that the 95% confidence upper limit on  $\sum m_\nu$  is nearly unchanged:  $\sum m_\nu < 0.44$  eV without clusters and  $\sum m_\nu < 0.38$  eV with clusters. This improvement is largely due to the tighter constraint on  $\sigma_8$  derived from the cluster data. The SPT<sub>CL</sub> data tightens the  $\sigma_8$  measurement from the CMB+BAO+ $H_0$  data from  $0.775 \pm 0.041$  to  $0.766 \pm 0.028$ .

We again compare these results to those reported by B11. B11 report  $\sigma_8 = 0.770 \pm 0.026$  and a 95% CL upper limit of  $\sum m_\nu < 0.33$  eV for the CMB+ $H_0$ +BAO+SPT<sub>CL</sub>(B11) data. The median  $\sigma_8$  value has shifted down slightly in this work leading to a higher  $\sum m_\nu$  limit. The parameter uncertainties are essentially unchanged.

### 7.4. Prospects for Further Improvement

The cosmological results in this paper are derived from a high-purity and high-redshift subsample of the catalog consisting of 100 galaxy clusters. The full SPT survey covers approximately 3.5 times the sky area used in this work and is being used to produce a similar high-purity catalog with 3.5 times as many clusters. Realizing the scientific potential of this sample will require significant improvements to the current mass calibration. We have simulated the impact of a more accurate mass calibration on both the current catalog and the full SPT survey. A 5% mass calibration would tighten the current constraints to  $\sigma(w) = 0.043$  (for CMB+BAO+ $H_0$ +SNe+SPT<sub>CL</sub>) and  $\sigma(\sum m_\nu) = 0.10$  eV (for CMB+BAO+ $H_0$ ) respectively, a factor of 1.3 better than those listed in Table 5 for the current mass calibration. Determining the mass calibration to better than 5% would have little impact with the current catalog. However, it would significantly improve constraints for the 3.5 times larger, full SPT sample and could make possible a significant detection of the sum of the neutrino masses.

As laid out by B11, four approved observation programs are being pursued by the SPT collaboration to independently test the cluster mass calibration, with the goal of reducing this uncertainty to a level  $\lesssim 5\%$ . First, X-ray observations with *Chandra* are scheduled for the 80 most-significant SPT cluster detections at  $z > 0.4$ . Second, we have been awarded time for weak lensing observations of  $\sim 35$  SPT-detected clusters spanning  $0.30 < z < 1.3$  using the Magellan and *Hubble* telescopes. Third, we have been awarded time for optical velocity dispersion observations of  $\sim 100$  SPT-detected clusters

using the Very Large Telescope (VLT) and a large NOAO program on Gemini South. Fourth, the DES will also yield weak lensing mass estimates ( $S/N \sim 1$ ) of all SPT cluster candidates. The combination of the X-ray, velocity dispersion, and weak lensing observations will enable valuable cross-checks between these different mass estimates and should lead to significant improvements in the cluster mass calibration.

## 8. CONCLUSIONS

We have presented a catalog of 224 cluster candidates detected with  $S/N$  greater than 4.5 in 720 deg<sup>2</sup> of the SPT survey. Using optical/NIR follow-up data, we have detected clear counterparts for 158 of these candidates, of which 135 were first identified as galaxy clusters in the SPT data. The observed purity of the full sample is 71%; the purity rises to 95% for the 121 candidates detected at a  $S/N$  greater than 5. We report photometric and in some cases spectroscopic redshifts for these galaxy clusters, finding redshifts between  $0.0552 < z < 1.37$  with a median redshift of  $z = 0.55$ . We also estimate the masses based on simulations and X-ray observations, and find the median mass of the sample is  $M_{500} = 3.3 \times 10^{14} M_\odot h_{70}^{-1}$ . This catalog expands the total number of published, optically confirmed galaxy clusters discovered with the SPT to 144 and triples the total number of SZ-discovered galaxy clusters.

We extend the cosmological fitting algorithm for SZ clusters presented by V10 and B11 in two ways. First, we implement an improved treatment of unconfirmed cluster candidates. This improvement has minimal impact given the high purity ( $\sim 95\%$ ) of the  $\xi > 5$  catalog. Second and more importantly, we develop a framework for combining cluster counts from fields observed with different noise levels, using simulations to recalibrate the SZ detection significance in each field. This framework will be essential for optimally analyzing the final SPT catalog.

We derive cosmological constraints based on the measured cluster abundances. In these analyses, we limit the cluster sample to the 100 cluster candidates detected with  $S/N \xi > 5$  and  $z > 0.3$  (or optically unconfirmed). Using just the information from these clusters and a BBN +  $H_0$  prior, we see a sizable improvement to the constraints on a  $\Lambda$ CDM cosmological model compared to the constraints reported in B11 with a smaller cluster sample and similar priors. However, when additional data (CMB+BAO+SNe) are added, the constraints from the cluster sample presented here are similar to those from B11. This is to be expected, because the B11 constraints were already limited by mass calibration uncertainty, not cluster sample size.

Adding the SPT cluster data to CMB+BAO+ $H_0$ +SNe data constrains the equation of state of dark energy to be  $w = -1.010 \pm 0.058$ . The uncertainty is a factor of 1.3 smaller than that without the SPT catalog and the preferred value remains consistent with a cosmological constant. The addition of SPT cluster data also reduces the uncertainty on  $\sigma_8$  in a  $w$ CDM cosmology by a factor of 1.4 from  $\sigma_8 = 0.840 \pm 0.038$  to  $\sigma_8 = 0.807 \pm 0.027$ .

We also use the measured SZ cluster counts to constrain  $\sigma_8$  and the sum of the neutrino masses. In an extension to the  $\Lambda$ CDM model that includes massive neutrinos, the SZ cluster counts tighten the  $\sigma_8$  constraint by a factor of 1.4 when added to the CMB+BAO+ $H_0$  data. This leads to a small preference for positive neutrino masses with  $\sum m_\nu = 0.17 \pm 0.13$  eV. The 95% confidence upper limit on the total neutrino mass slightly decreases from 0.44 eV to 0.38 eV. The relative improvement

to the upper limit is less than would be expected because of the preference for higher neutrino masses.

The SPT survey of 2500 deg<sup>2</sup> was completed in 2011 November. The survey area, comprising 6% of the total sky, has been mapped to depths of approximately 40, 18, and 70  $\mu\text{K}_{\text{CMB}}$ -arcmin at 95, 150, and 220 GHz respectively. These depths are roughly equal to those of the 2009 data presented here. The survey should detect  $\sim 550$  optically confirmed galaxy clusters at  $S/N \xi > 4.5$ , with a median redshift of  $\sim 0.5$  and a median mass of  $M_{500} \sim 3 \times 10^{14} M_{\odot} h_{70}^{-1}$ . Ongoing X-ray, weak lensing, and optical velocity dispersion observations of SPT SZ-selected clusters will be used to produce an improved cluster mass calibration of the sample. The full SPT survey and improved mass calibration will lead to constraints on the dark energy equation of state,  $w$ , better than current constraints from the combination of CMB+BAO+SNe data and will provide an independent systematic test of the standard dark energy paradigm by measuring the effect of dark energy on the growth of structure. Furthermore, the combination of CMB+BAO+SNe constraints with those from the full SPT cluster sample will break parameter degeneracies that exist in either data set alone, resulting in significantly tighter constraints on dark energy. The addition of the SPT cluster abundance data is also already leading to tighter constraints on the sum of the neutrino masses; with the ongoing program to improve the cluster mass calibration, it may be possible to produce a significant detection of non-zero neutrino mass.

The South Pole Telescope program is supported by the National Science Foundation through grant ANT-0638937. Partial support is also provided by the NSF Physics Frontier Center grant PHY-0114422 to the Kavli Institute of Cosmological Physics at the University of Chicago, the Kavli Foundation, and the Gordon and Betty Moore Foundation. Galaxy cluster research at Harvard is supported by NSF grant AST-1009012. Galaxy cluster research at SAO is supported in part by NSF grants AST-1009649 and MRI-0723073. The McGill group acknowledges funding from the National Sciences and Engineering Research Council of Canada, Canada Research Chairs program, and the Canadian Institute for Advanced Research. X-ray research at the CfA is supported through NASA Contract NAS 8-03060. This work is based in part on observations made with the *Spitzer Space Telescope*, which is operated by the Jet Propulsion Laboratory, California Institute of Technology under a contract with NASA. Support for this work was provided by NASA through an award issued by JPL/Caltech. The Munich group acknowledges support from the Excellence Cluster Universe and the DFG research program TR33. R.J.F. is supported by a Clay Fellowship. B.A.B is supported by a KICP Fellowship, M. Bautz acknowledges support from contract 2834-MIT-SAO-4018 from the Pennsylvania State University to the Massachusetts Institute of Technology. M.D. acknowledges support from an Alfred P. Sloan Research Fellowship, W.F. and C.J. acknowledge support from the Smithsonian Institution, and B.S. acknowledges support from the Brinson Foundation.

Support for X-ray analysis was provided by NASA through Chandra Award Numbers 12800071, 12800088, and G02-13006A issued by the Chandra X-ray Observatory Center, which is operated by the Smithsonian Astrophysical Observatory for and on behalf of NASA under contract NAS8-03060. Optical imaging data from the Blanco 4 m at Cerro Tololo Inter-American Observatories (programs 2005B-0043, 2009B-0400, 2010A-0441, and 2010B-0598) and spectroscopic observations

from VLT programs 086.A-0741 and 286.A-5021 and Gemini program GS-2009B-Q-16 were included in this work. Additional data were obtained with the 6.5 m Magellan Telescopes located at the Las Campanas Observatory, Chile.

We acknowledge the use of the Legacy Archive for Microwave Background Data Analysis (LAMBDA). Support for LAMBDA is provided by the NASA Office of Space Science. This research used resources of the National Energy Research Scientific Computing Center, which is supported by the Office of Science of the U.S. Department of Energy under Contract No. DE-AC02-05CH11231. This research has made use of the SIMBAD database, operated at CDS, Strasbourg, France, and the NASA/IPAC Extragalactic Database (NED) which is operated by the Jet Propulsion Laboratory, California Institute of Technology, under contract with the National Aeronautics and Space Administration.

*Facilities:* Blanco (MOSAIC, NEWFIRM), CXO (ACIS), Gemini:South (GMOS), Magellan:Baade (IMACS), Magellan: Clay (LDSS3), *Spitzer* (IRAC), SPT, Swope (CCD), *XMM* (EPIC)

## REFERENCES

- Abell, G. O., Corwin, H. G., Jr., & Olowin, R. P. 1989, *ApJS*, **70**, 1
- Ahmad, Q. R., Allen, R. C., Andersen, T. C., et al. 2002, *PhRvL*, **89**, 011301
- Allen, S. W., Evrard, A. E., & Mantz, A. B. 2011, *ARA&A*, **49**, 409
- Amanullah, R., Lidman, C., Rubin, D., et al. 2010, *ApJ*, **716**, 712
- Andersson, K., Benson, B. A., Ade, P. A. R., et al. 2011, *ApJ*, **738**, 48
- Ashby, M. L. N., Stern, D., Brodwin, M., et al. 2009, *ApJ*, **701**, 428
- Ashie, Y., Hosaka, J., Ishihara, K., et al. 2004, *PhRvL*, **93**, 101801
- Barbosa, D., Bartlett, J., Blanchard, A., & Oukbir, J. 1996, *A&A*, **314**, 13
- Battye, R. A., & Weller, J. 2003, *PhRvD*, **68**, 083506
- Beers, T. C., Flynn, K., & Gebhardt, K. 1990, *AJ*, **100**, 32
- Benson, B. A., de Haan, T., Dudley, J. P., et al. 2011, *ApJ*, in press (arXiv:1112.5435)
- Böhringer, H., Schuecker, P., Guzzo, L., et al. 2004, *A&A*, **425**, 367
- Brodwin, M., Ruel, J., Ade, P. A. R., et al. 2010, *ApJ*, **721**, 90
- Buckley-Geer, E. J., Lin, H., Drabek, E. R., et al. 2011, *ApJ*, **742**, 48
- Carlstrom, J. E., Ade, P. A. R., Aird, K. A., et al. 2011, *PASP*, **123**, 568
- Carlstrom, J. E., Holder, G. P., & Reese, E. D. 2002, *ARA&A*, **40**, 643
- Cash, W. 1979, *ApJ*, **228**, 939
- Cavaliere, A., & Fusco-Femiano, R. 1976, *A&A*, **49**, 137
- Collister, A. A., & Lahav, O. 2004, *PASP*, **116**, 345
- Dalton, G. B., Efstathiou, G., Maddox, S. J., & Sutherland, W. J. 1994, *MNRAS*, **269**, 151
- Dalton, G. B., Maddox, S. J., Sutherland, W. J., & Efstathiou, G. 1997, *MNRAS*, **289**, 263
- de Grandi, S., Böhringer, H., Guzzo, L., et al. 1999, *ApJ*, **514**, 148
- Desai, S., Armstrong, R., Mohr, J. J., et al. 2012, *ApJ*, **757**, 83
- de Zotti, G., Ricci, R., Mesa, D., et al. 2005, *A&A*, **431**, 893
- Duus, A., & Newell, B. 1977, *ApJS*, **35**, 209
- Ebeling, H., Voges, W., Böhringer, H., et al. 1996, *MNRAS*, **281**, 799
- Eguchi, K., Enomoto, S., Furuno, K., et al. 2003, *PhRvL*, **90**, 021802
- Eikenberry, S., Elston, R., Raines, S. N., et al. 2006, *Proc. SPIE*, **6269**, 626917
- Fetisova, T. S. 1981, *SvA*, **25**, 647
- Foley, R. J., Andersson, K., Bazin, G., et al. 2011, *ApJ*, **731**, 86
- Haiman, Z., Mohr, J. J., & Holder, G. P. 2001, *ApJ*, **553**, 545
- Hamann, J., Lesgourgues, J., & Mangano, G. 2008, *JCAP*, **03**, 004
- High, F. W., Stalder, B., Song, J., et al. 2010, *ApJ*, **723**, 1736
- Holder, G., Haiman, Z., & Mohr, J. J. 2001, *ApJL*, **560**, 111
- Holder, G. P., & Carlstrom, J. E. 2001, *ApJ*, **558**, 515
- Kalberla, P., Burton, W., Hartmann, D., et al. 2005, *A&A*, **440**, 775
- Keisler, R., Reichardt, C. L., Aird, K. A., et al. 2011, *ApJ*, **743**, 28
- Kirkman, D., Tytler, D., Suzuki, N., O'Meara, J. M., & Lubin, D. 2003, *ApJS*, **149**, 1
- Komatsu, E., Smith, K. M., Dunkley, J., et al. 2011, *ApJS*, **192**, 18
- Lewis, A., & Bridle, S. 2002, *PhRvD*, **66**, 103511
- Lewis, A., Challinor, A., & Lasenby, A. 2000, *ApJ*, **538**, 473
- Lima, M., & Hu, W. 2007, *PhRvD*, **76**, 123013
- Lueker, M., Reichardt, C. L., Schaffer, K. K., et al. 2010, *ApJ*, **719**, 1045
- Mantz, A., Allen, S. W., Ebeling, H., Rapetti, D., & Drlica-Wagner, A. 2010, *MNRAS*, **406**, 1773

- Marriage, T. A., Acquaviva, V., Ade, P. A. R., et al. 2011, *ApJ*, **737**, 61
- Melin, J.-B., Bartlett, J. G., & Delabrouille, J. 2006, *A&A*, **459**, 341
- Menanteau, F., Hughes, J. P., Barrientos, L. F., et al. 2010, *ApJS*, **191**, 340
- Miknaitis, G., Pignata, G., Rest, A., et al. 2007, *ApJ*, **666**, 674
- Mohr, J. J., Adams, D., Barkhouse, W., et al. 2008, *Proc. SPIE*, Vol. **7016**, 70160L
- Molnar, S. M., Haiman, Z., Birkinshaw, M., & Mushotzky, R. F. 2004, *ApJ*, **601**, 22
- Motl, P. M., Hallman, E. J., Burns, J. O., & Norman, M. L. 2005, *ApJL*, **623**, 63
- Murphy, T., Sadler, E. M., Ekers, R. D., et al. 2010, *MNRAS*, **402**, 2403
- Padin, S., Staniszewski, Z., Keisler, R., et al. 2008, *ApOpt*, **47**, 4418
- Papovich, C. 2008, *ApJ*, **676**, 206
- Percival, W. J., Reid, B. A., Eisenstein, D. J., et al. 2010, *MNRAS*, **401**, 2148
- Perlmutter, S., Aldering, G., Goldhaber, G., et al. 1999, *ApJ*, **517**, 565
- Piffaretti, R., Arnaud, M., Pratt, G. W., Pointecouteau, E., & Melin, J.-B. 2011, *A&A*, **534**, A109
- Planck Collaboration, Ade, P. A. R., Aghanim, N., et al. 2011, *A&A*, **536**, A8
- Quintana, H., & White, R. A. 1990, *Ap&SS*, **173**, 265
- Reichardt, C. L., Shaw, L., Zahn, O., et al. 2012, *ApJ*, **755**, 70
- Rest, A., Stubbs, C., Becker, A. C., et al. 2005, *ApJ*, **634**, 1103
- Riess, A. G., Filippenko, A. V., Challis, P., et al. 1998, *AJ*, **116**, 1009
- Riess, A. G., Macri, L., Casertano, S., et al. 2011, *ApJ*, **730**, 119
- Rozo, E., Wechsler, R. H., Rykoff, E. S., et al. 2010, *ApJ*, **708**, 645
- Ruhl, J., Ade, P. A. R., Carlstrom, J. E., et al. 2004, *Proc. SPIE*, **5498**, 11
- Schaffer, K. K., Crawford, T. M., Aird, K. A., et al. 2011, *ApJ*, **743**, 90
- Sehgal, N., Bode, P., Das, S., et al. 2010, *ApJ*, **709**, 920
- Sérsic, J. L. 1974, *Ap&SS*, **28**, 365
- Shaw, L. D., Nagai, D., Bhattacharya, S., & Lau, E. T. 2010, *ApJ*, **725**, 1452
- Shimon, M., Sadeh, S., & Rephaeli, Y. 2011, *MNRAS*, **412**, 1895
- Shirokoff, E., Reichardt, C. L., Shaw, L., et al. 2011, *ApJ*, **736**, 61
- Sifton, C., Menanteau, F., Hasselfield, M., et al. 2012, *ApJ*, submitted (arXiv:1201.0991)
- Song, J., Mohr, J. J., Barkhouse, W. A., Warren, M. S., & Rude, C. 2012a, *ApJ*, **747**, 58
- Song, J., Zenteno, A., Stalder, B., et al. 2012b, *ApJ*, **761**, 22
- Staniszewski, Z., Ade, P. A. R., Aird, K. A., et al. 2009, *ApJ*, **701**, 32
- Stern, D., Eisenhardt, P., Gorjian, V., et al. 2005, *ApJ*, **631**, 163
- Story, K., Aird, K. A., Andersson, K., et al. 2011, *ApJ*, **735**, L36
- Struble, M. F., & Rood, H. J. 1999, *ApJS*, **125**, 35
- Šuhada, R., Song, J., Böhringer, H., et al. 2010, *A&A*, **514**, L3
- Sunyaev, R., & Zel'dovich, Y. 1980, *ARA&A*, **18**, 537
- Sunyaev, R. A., & Zel'dovich, Y. B. 1972, *CoASP*, **4**, 173
- Tinker, J., Kravtsov, A. V., Klypin, A., et al. 2008, *ApJ*, **688**, 709
- Vanderlinde, K., Crawford, T. M., de Haan, T., et al. 2010, *ApJ*, **722**, 1180
- van Engelen, A., Keisler, R., Zahn, O., et al. 2012, *ApJ*, **756**, 142
- Vieira, J. D., Crawford, T. M., Switzer, E. R., et al. 2010, *ApJ*, **719**, 763
- Vikhlinin, A., Burenin, R. A., Ebeling, H., et al. 2009a, *ApJ*, **692**, 1033
- Vikhlinin, A., Kravtsov, A. V., Burenin, R. A., et al. 2009b, *ApJ*, **692**, 1060
- Voges, W., Aschenbach, B., Boller, Th., et al. 1999, *A&A*, **349**, 389
- Voges, W., Aschenbach, B., Boller, Th., et al. 2000, The *ROSAT* All-Sky Survey Faint Source Catalog (Strasbourg: CDS)
- Wang, L., & Steinhardt, P. J. 1998, *ApJ*, **508**, 483
- Wang, S., Haiman, Z., Hu, W., Khoury, J., & May, M. 2005, *PhRvL*, **95**, 011302
- Wang, S., Khoury, J., Haiman, Z., & May, M. 2004, *PhRvD*, **70**, 123008
- Williamson, R., Benson, B. A., High, F. W., et al. 2011, *ApJ*, **738**, 139